# HIGH-SPEED FLOW VISUALIZATION AND IR IMAGING OF POOL BOILING ON SURFACES HAVING DIFFERING DYNAMIC WETTABILITIES

by

**Nicholas T. Vu**

**A Thesis**

*Submitted to the Faculty of Purdue University*

*In Partial Fulfillment of the Requirements for the degree of*

**Master of Science in Mechanical Engineering**


School of Mechanical Engineering

West Lafayette, Indiana

December 2020

# THE PURDUE UNIVERSITY GRADUATE SCHOOL
# STATEMENT OF COMMITTEE APPROVAL

**Dr. Justin A. Weibel, Chair**

School of Mechanical Engineering

**Dr. Peter A. Bermel**

School of School of Electrical and Computer Engineering

**Dr. Terrence R. Meyer**

School of Mechanical Engineering

**Approved by:**

Dr. Nicole L. Key

*For those before me*

# ACKNOWLEDGMENTS

I would first like to thank the Purdue Military Research Initiative for giving me the opportunity to pursue my Master of Science at Purdue while active duty. Furthermore, PMRI is what got me interested in research in the first place with the Midshipman/Cadet Introduction to Research Program. I would also like to thank the ONR NEPTUNE program for funding many aspects of this research.

I would also like to thank my committee—Prof. Bermel, and Prof. Meyer, and Prof. Weibel—for being flexible and spending the time to serve on my board. I appreciate any feedback given. I also appreciate all the feedback and mentorship that Prof. Weibel has given me as my advisor throughout my time here at Purdue.

Many lab members, both current and former, have been instrumental to this project as well. Dr. Taylor Allred laid the groundwork for much of what is presented here. Dr. Julian Castillo helped with various aspects of the infrared camera. Rishav Roy and Manohar Bongarala helped with the sample fabrication. Soumya Bandyopadhyay helped with various aspects of modeling.

Thank you to those who supported me throughout. Prof. Warzoha from the Naval Academy really helped me get into research and to Purdue. I would also like to thank my family and friends for uplifting my spirits when I felt down. Thanks mom and dad for being my biggest fans and for inspiring me to become the person I am today. I would not have been able to make it without your continual support. Also, thanks to Chris for being a great older brother and for being the best role model I could have. Thanks to Colby Bowers for mentoring me in my professional life. And finally, I would like to acknowledge my wonderful girlfriend, Monika, for everything she has done and for serving our great country on the front lines.

# TABLE OF CONTENTS

# LIST OF TABLES

# LIST OF FIGURES

# ABSTRACT

Boiling is used in a wide variety of industries, including electronics cooling, distillation, and power generation. Fundamental studies on the boiling process are needed for effective implementation. Key performance characteristics of boiling are the heat transfer coefficient, which determines the amount of heat flux that can be dissipated for a given superheat, and critical heat flux (CHF), the failure point that occurs when vapor blankets the surface. The wettability of a surface is one of the key parameters that affects boiling behavior. Wetting surfaces (e.g., hydrophilic surfaces), typically characterized by a static contact angle below 90°, have better critical heat flux due to effective rewetting, but compromised heat transfer coefficients due to increased waiting times between nucleation of each bubble. Meanwhile, nonwetting surfaces (e.g., hydrophobic surfaces), characterized by static contact angles greater than 90°, have better heat transfer coefficients due to improved nucleation characteristic, but reach critical heat flux early due to surface dryout. However, recent studies have shown that the static contact angle alone offers and incomplete, and sometimes inaccurate, description of this behavior, which is instead governed entirely by the dynamic wettability. Specifically, the receding contact angle impacts the size and contact area of bubbles forming on a surface during boiling, while the advancing contact angle determines how the bubble departs. With this more complete set of wettability descriptors, three characteristic wetting regimes define the boiling behavior: hygrophilic surfaces having advancing and receding contact angles both under 90°; hygrophobic surfaces having both these dynamic contact angles over 90°; and ambiphilic surfaces having a receding contact angle less than 90°, but an advancing contact angle greater than 90°. The goal of this thesis is to experimentally characterize and compare the behavior of boiling surfaces in each of these regimes, observe the contact line behavior, and explain the mechanisms for their differences in performance.

Using high-speed infrared (IR) thermography of the surface along with side-view high-speed visualization, the key boiling characteristics of each wettability regime were studied in a pool boiling facility. The infrared camera allowed for mapping of the surface temperatures as viewed from below, revealing nucleation phenomenon near the surface that are not possible to ascertain by the traditional high-speed visualization. Departing bubbles are observed to grow at a constant receding angle, pin at the maximum contact diameter, and depart the surface as the liquid-vapor interface moved at the advancing contact angle. For the surfaces having advancing contact

angles > 90°, a pinched-off remnant of the bubble remains on the surface and promotes immediate growth of a subsequent bubble, without any waiting period required for renucleation. The boiling curves calculated from averaging the surface temperatures recorded using the IR camera indicated that the ambiphilic surface offered the lowest surface temperatures of all wettability regimes, without having the drawback of a premature CHF. The first-of-their-kind IR visualizations of the surface temperatures during boiling from ambiphilic surfaces revealed that this was attributed to an order of magnitude increase in the nucleation site density, short ebullition and waiting times, and very small contact diameters for individual bubbles. The favorable nucleation characteristics allow for efficient heat transfer during bubble formation, while the pinned contact line (and thereby small contact diameter) prevents vapor spreading over the surface and critical heat flux. In contrast, the hygrophobic surface performed well at low heat fluxes due to similarly favorable nucleation characteristics but reached critical heat flux at very low heat fluxes. This premature CHF was due to the long ebullition times, large contact diameters, and dryout underneath the bubbles, as evidenced by the hot spots that formed. Finally, the hygrophilic surface had the worst overall heat transfer coefficient at low heat fluxes but was able to avoid critical heat flux similar to the ambiphilic surface. Both of these performance traits are attributed to the complete surface rewetting that occurred between each successive bubble nucleation, which leads to long waiting times between each nucleation but prevents vapor coverage.

High-speed visualization and IR thermography provided critical insight into the role of dynamic wettability in boiling. The bubble dynamics and local surface temperature profile were monitored to explore the different mechanisms of heat transfer in each of the wetting regimes and how bubble morphology affects the local heat transfer and CHF.

# 1. INTRODUCTION

## 1.1 Background

Boiling is used for a wide variety of industries, from relatively simple applications such as cooking to the foundation of generating electric power with steam turbines, creating drinkable water by distillation in desalination plants, and heating/cooling through vapor-compression refrigeration cycles. In particular, boiling is a topic of interest for electronics cooling applications due to its ability to leverage the latent heat of vaporization during phase change from liquid to vapor to efficiently dissipate large heat fluxes with low to modest increases in surface temperature [1], [2]. Electronics cooling needs have become more pressing and extreme of an issue due to the continual trends towards more power-dense devices that generate higher heat fluxes [3]. Thermal management is one of the primary constraints to increasing computer processor performance [4] and the cause of more than 50% of integrated circuit failures [5]. Moreover, the cooling of electronics can use large amounts of energy. For example, data centers consumed 1.8% of all electricity in 2014 [6], with over 30% of that energy consumption being used for cooling [7]. Although two-phase cooling technologies have the potential to meet many of these needs and have been used practically in many applications, many aspects of boiling with regards to performance and predictability are not well understood due to the complex relationship between mass and energy transfer at the solid-vapor-liquid contact line. A better fundamental understanding of the boiling process is needed to facilitate its widespread adoption.

Two-phase thermal management technologies typically rely on boiling that occurs either in a stagnant pool (also known as pool boiling or immersion cooling) or with an induced flow (e.g., internal flow boiling in microchannels or external flow boiling in jet impingement). Pool boiling is the simplest scenario, as it is a mostly passive system that relies on buoyancy forces and gravity to circulate the coolant. Many fundamental studies of boiling heat transfer are performed in stagnant pools as it is the simplest foundational situation, without the added transport complexities of flow boiling. This thesis will investigate a pool boiling from a flat surface to understand the effects of dynamic surface wettability on the boiling process; the same fundamental learnings can be extended to more complex scenarios having different surface geometries or active flow.

Effective heat transfer using pool boiling often occurs within a nucleate boiling regime between the beginning of bubble formation (onset of nucleate boiling, ONB) and critical heat flux (CHF). The boiling regimes are shown in the boiling curve and visualizations in Fig. 1.1. Prior to ONB, single phase natural convection is responsible for heat transfer. Critical heat flux is the sudden transition from nucleate boiling to film boiling, causing a dramatic decrease in heat transfer efficiency and a sudden increase in surface temperature. This is due to the formation of a vapor film insulating the surface. Critical heat flux, also known as burnout, is the failure point for boiling applications. One of the key goals for boiling enhancement is increasing the CHF, which would allow higher heat fluxes to be dissipated. A second objective for boiling enhancement is to increase the heat transfer coefficient, which measures how much heat flux can be dissipated for a given surface temperature rise above the saturation temperature. On a boiling curve, improved performance therefore corresponds with an upward shift in heat flux or leftward decrease in the surface temperature.

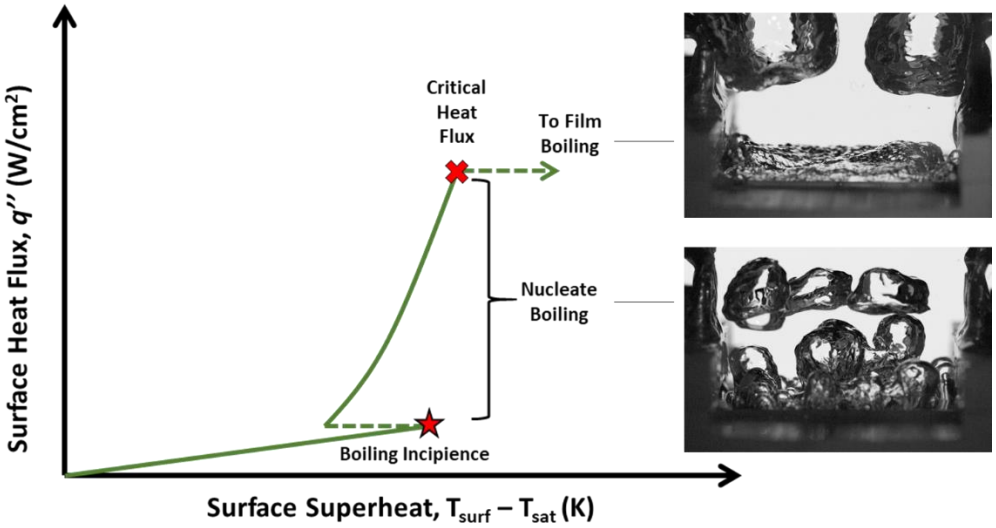


Figure 1.1. Example of a boiling curve.

Methods of improving CHF and heat transfer coefficient for pool boiling have been divided into active and passive technologies [8]. Active technologies for pool boiling (e.g., mechanical mixing, vibration, electrostatic fields) have been shown to be effective, but are impractical in many settings due to cost, size, and energy limitations. Meanwhile, passive technologies—which focus on modifying the fluid, operating conditions, and surface—have also been able to successfully improve boiling performance. The primary focus of this thesis on those techniques that aim to

affect the boiling process through surface modifications, and more specifically, the wettability of the surface. Traditional understanding of the effects of wettability on boiling is that the CHF and heat transfer coefficient often come with a tradeoff: wetting surfaces characterized by static contact angles below 90° have better CHF but worse heat transfer coefficient [9]–[12], while nonwetting surfaces characterized by static contact angles above 90° have better heat transfer coefficient but worse CHF [11], [13], [14]. Because of this early onset of CHF, nonwetting surfaces have largely been overlooked as a route toward performance enhancement.

However, recent studies by Allred et al. [15]–[17] have challenged the traditional understanding of wettability on boiling performance by showing boiling improvement via parahydrophobic surfaces that have high static contact angles. These studies found that dynamic contact wettability determines the boiling characteristics of a surface, not the typical framework for understanding founded on static contact angles. Numerical simulations performed considering the dynamic contact line behavior [17] were used to redefine three regimes of wettability in the context of boiling. Hygrophilic systems are characterized by receding and advancing contact angles both below 90°, which were proposed to have higher heat transfer per bubble but poor nucleation characteristics. Hygrophobic systems characterized by receding and advancing contact angles both above 90° were proposed to form hot spots under each bubble and have poor critical heat flux performance. In these regime definitions, the prefix “hygro-” is used for generality to all potential fluid (versus the prefix hydro-that is specific to water). A third ambiphilic wetting regime is characterized by a receding contact angle below 90° and an advancing contact angle above 90°. These regimes were postulated to offer less heat transfer per bubble but better nucleation characteristics when compared with hygrophilic systems, making it unclear which would offer a net benefit in overall boiling heat transfer. The prefix “ambi-” meaning “both” is used to describe these surface—fluid systems that have an attraction to both the liquid via low receding contact angle and vapor via high advancing contact angle. Note that the advancing receding contact angle must strictly be larger than the receding contact angle (hence there is no regime with a receding contact angle above 90° and an advancing contact angle below 90°).

## 1.2 Objectives

The goal of this study is to explore the effects of dynamic wettability on pool boiling heat transfer. This is accomplished by performance pool boiling tests on surfaces having wetting

behaviors representative of these three newly identified regimes: hygrophilic, hygrophobic, and ambiphilic. Using high-speed side-view flow visualization and infrared thermography, the bubble dynamics and local surface temperature profile are monitored to explore the different mechanisms of heat transfer, bubble morphologies, and heat transfer performance in each of the wetting regimes.

## 1.3 Organization

This thesis is organized in chapters as follows. Chapter 1 provides the background, motivation, and contributions of this work. Chapter 2 provides a literature review on pool boiling, boiling heat transfer mechanisms, surface wettability, and infrared thermography for pool boiling. Chapter 3 provides the methodology, including information on the sample fabrication, boiling facility, and data processing. Chapter 4 provides the results and discussions of the boiling characteristics of surface-fluid systems within the hygrophilic, hygrophobic, and ambiphilic regimes. Finally, Chapter 5 provides the conclusions of the work and suggested topics for future study.

# 2. LITERATURE REVIEW

This chapter provides a review of the literature pertinent for this dissertation, including pool boiling, effects of wettability on boiling, the use of infrared thermography for pool boiling studies, and bubble ebullition.

## 2.1 Mechanisms and Models for Boiling Heat Transfer

Heat transfer during boiling revolves around the bubble ebullition cycle, which consists of a waiting period, nucleation, growth, and departure. During this cycle, a wide variety of proposed heat transfer mechanisms occur. Heat transfer can occur through evaporation of a thin liquid layer between a growing bubble and the surface known as the microlayer, evaporation of superheated vapor around the bubble, evaporation at the three-phase contact line after partial dryout of the microlayer, micro-convection due to perturbations of the bubble, transient conduction as the dry patch is rewet with subcooled liquid, and background natural convection between the bubble nucleation sites [18]. With the wide variety of heat transfer mechanisms that can occur during the bubble ebullition cycle, a wide variety of theories for prediction exist without a clear consensus.

Many early theories did not consider cooling by phase change, but instead focused on enhanced single-phase convection that occurs as a bubble departs and agitates the fluid in its wake. The most well-known model that is still widely used today is Rohsenow's correlation [19], which considers the bubble departure diameter from Fritz's correlation and a characteristic bubble velocity [20]:

$$\frac{q_s''}{\mu_l h_{fg}}\left[\frac{\sigma}{g(\rho_l-\rho_v)}\right]^{\frac{1}{2}} = \left(\frac{1}{C_{sf}}\right)^3 Pr_l^{-3n}\left[\frac{C_{p,l}(T_s-T_{sat})}{h_{fg}}\right]^3, \tag{2.1}$$

where $q_s''$ is the heat flux, $\mu_l$ is the kinematic viscosity of the fluid, $h_{fg}$ is the latent heat of vaporization, $\sigma$ is the interfacial tension, $g$ is acceleration due to gravity, $\rho_l - \rho_v$ is the difference in density between the liquid and vapor phases, $\mathrm{Pr}_l$ is Prandtl number of the liquid, $C_{p,l}$ is the liquid specific heat, $T_s - T_{sat}$ is the superheat, and n is either 1 for water or 1.7 for any other fluid. $C_{sf}$ is a constant that depends on the fluid-surface combination, defined by:

$$C_{sf} = \frac{C_b \theta \sqrt{2}}{A}, \tag{2.2}$$

where $C_b$ is a constant, $\theta$ is the contact angle, and $A$ is the cross-sectional area. Other microconvection models include those by Forster and Grief [21] and Forster and Zuber [22]. Although these correlations are older, more recent experimental studies by Jung et al. [23] have found that heat transfer by convection was much larger than contact line heat transfer, accounting for as much as 85% of the total heat transfer at CHF. This suggests there is some validity in using models based on microconvection and bubble agitation.

Another prominent modeling approach are those based on transient conduction, such as by Mikic and Rohsenow [24]. These models consider microlayer evaporation and bubble agitation as potential heat transfer mechanisms but argue that transient conduction is the single most important contributor to heat transfer. Here, as the bubble departs it takes with it a superheated region twice the bubble diameter that is renewed with saturated liquid during the waiting time. This model predicts that there would be a spatially uniform heat transfer after bubble departure twice the bubble departure diameter that decays during the regrowth [18].

Moore and Mesler [25] were among the first to suggest that microlayer heat transfer was responsible for the majority of the heat transfer at high heat fluxes. They observed a sudden 11-17 °C drop in surface temperature over 2 ms at high heat fluxes by using an extremely rapid response thermocouple and concluded that microlayer heat transfer accounted for 70-90% of the average heat flux during the temperature drop. These temperature drops would not be as dramatic given only bubble agitation. Experimental studies such as the laser interferometric measurements of Chen et al [26], [27] have confirmed the presence of the microlayer in the entirety of the nucleate boiling regime for experiments performed on wetting surfaces. Various other researchers have found the contribution of microlayer evaporation to heat transfer with a range of results. Jung and Kim [23] found microlayer evaporation contributed 17% of the total heat transfer using total reflection, laser interferometry, infrared thermography, and high-speed imaging. Utaka et al [28] found that the microlayer contributed 39% for ethanol and 14-44% for water. Judd and Hwang [29] concluded that microlayer evaporation contributed up to one-third of the total heat transfer at the largest heat flux studied.

Another prominent mechanism is heat transfer at the contact line. Wagner et al. [30] proposed that a large amount of heat transfer can occur near the three-phase contact line because

of the very thin film due to the stretching of the meniscus. Stephan and Hammer [31] studied the micro-region near the three-phase contact line and the macro-region away from the contact line, and they found that the majority of the heat flux during boiling occurred from the micro-region. Wagner and Stephan [32], using infrared thermography, found large amounts of heat flux going through the microregion near the three-phase-contact line. This study decomposed bubble growth into three stages. The first stage is characterized by a few milliseconds of rapid growth and the largest heat transfer, 30% of which occurs through the microregion. The second stage begins as the bubble reaches the maximum diameter and begins to constrict, with dynamic contact angle changing from receding to advancing. During this stage, the microregion accounts for less than 10% of the bubble heat transfer, and although the reason is not fully understood, they theorize it may be related to the low contact-line movement. Finally, the third stage is characterized by bubble departure at the advancing contact angle, which has the lowest overall heat transfer but second maximum in heat transfer through the microregion, which accounted for 40-60%.

Many models consider multiple mechanisms and have run experiments to determine the contribution of each. For example, Moghaddam and Kiger [33], [34] conducted FC-72 boiling experiments with heat flux sensors and created a composite model incorporating microlayer evaporation, transient conduction, and microconvection. They found that microlayer evaporation was the smallest contribution that decreased with increased surface temperature (28.8% to 16.3% from 80 °C to 97 °C), transient conduction had the highest contribution at low surface temperatures but decreased at higher temperatures (45.4% to 32.1% from 80 °C to 97 °C), and microconvection had the least contribution at low temperatures and the highest at high temperatures (25.8% to 51.6% from 80 °C to 97 °C). Yabuki and Nakabeppu [35] used a micro-electro-mechanical (MEMS) sensor consisting of two film resistance temperature detectors to directly measure wall superheat, 11 thin film thermocouples to measure temperature variation, and an electrolysis trigger to promote nucleation. They found that microlayer evaporation increased to a maximum value of 60% and decrease to almost 0% until departure as the dry-out region increased.

### 2.1.1 Models for Critical Heat Flux

With the occurrence critical heat flux being one of the key concerns for boiling applications, its mechanism and models for prediction have been studied and reviewed extensively [36], [37], including over a thousand empirical correlations for CHF [38], [39]. Due to the vast quantity of

different models, this section will only briefly discuss some of the more widely used theories and models.

The widely recognized model is that proposed by Zuber [40], [41], which is based on a hydrodynamic instability theory that only depends on fluid properties and is independent of surface characteristics. It was proposed that at high heat fluxes, the large rates of evaporation cause the velocity of the vapor leaving the surface to be large, causing the combined effects of the Taylor and Helmholtz instabilities to become significant. The system was modeled as having a cellular arrangement of separate vapor jets formed due to the Taylor instability, with a width half of a Taylor wavelength and the distance between jets at a Taylor wavelength. At a critical velocity, these jets become Helmholtz unstable due to velocity differences between the vapor and liquid, ultimately causing a vapor mushroom that prevents rewetting of the surface. Zuber's CHF model takes the form:

$$q_{chf} = K\rho_v h_{fg}\left[\frac{\sigma g(\rho_l-\rho_v)}{\rho_v^2}\right]^{\frac{1}{4}}, \tag{2.3}$$

where K is a numerical constant bounded between 0.119 and 0.157 due to assumptions concerning the spectrum of unstable disturbances, with Zuber recommending an approximate mean of $\pi/24$, or 0.131. Many correlations based on Zuber's model have been formed to incorporate surface effects, such as contact angle and roughness by Kim et al [42]. An extensive list can be found in Ref. [36]. While the foundational mechanisms underlying Zuber's model have been greatly debated, it often provides a reasonably accurate prediction for many systems.

Various other mechanisms for CHF have been considered as well, including some that predate Zuber. Rohsenow and Griffith [43] proposed that bubble coalescence was the cause of CHF. They also proposed that size and frequency of bubbles departing the surface are independent of heat flux, but the number of nucleation sites increases with heat flux. Eventually, bubble spacing becomes so small that neighboring bubbles join and blanket the surface with vapor. Another theory based on microlayer dryout was proposed by Haramura and Katto [44]. In this model, vapor stems across the liquid microlayer to feed a large, coalesced bubble that formed due to the Helmholtz instability, and CHF occurs as this bubble grows due to evaporation of the microlayer. Models proposed by Yagov [45] and Theofanous et al. [46] propose that the mechanism for CHF is the formation of a hot/dry spot, which grows irreversibly and fails to rewet.

Therefore, CHF is a function of viscosity, and the ability for previous hydrodynamic models to predict experimental data were only possible due to weak viscosity effects in the fluids tested. Another model, the interfacial lift-off model, proposes that CHF occurs when the momentum of the vapor lifts the bulk liquid away from the surface and prevents rewetting [47], [48].

## 2.2 Surface Wettability

Surface modifications have long been known to impact the boiling process with an extensive library of studies on aspects such as roughening [42], [49]–[53], porous coatings [54]–[57], and micro-structures [58]–[60]. Although these viable alternative methods exist, this review will focus on surface wettability and how it has been used to improve boiling performance.

### 2.2.1 Wettability

Wettability describes a liquid's ability to adhere to a solid surface. Wettability is commonly characterized by contact angle, which is the angle between the liquid-vapor interface and solid-liquid interface for a droplet viewed from its side. The contact angle for an ideal, smooth surface is defined by Young's equation [61]:

$$\gamma_{lv} cos(\theta_E) = \gamma_{sv} - \gamma_{sl}, \tag{2.4}$$

where $\theta_E$ is the equilibrium contact angle, $\gamma_{lv}$ is the liquid-vapor interfacial tension, $\gamma_{sv}$ is the solid-vapor interfacial tension, and $\gamma_{sl}$ is the solid-liquid interfacial tension. In practice, real surfaces have an associated static contact angle and two dynamic contact angles, namely, the receding and advancing contact angles. Contact angles are typically measured by gently placing a sessile drop on a surface and measuring the three-phase contact line, typically with a tool known as a goniometer. The static contact angle is measured on horizontal surface for a quasi-steady, nonmoving droplet. The dynamic contact angles are measured during contact line motion, with receding being the minimum possible angle and advancing the highest. This contact line motion can be induced experimentally by tilting the surface until movement or by altering the volume. In the former method, the surface tilt is increased slowly until the drop begins to move, and the leading edge is the advancing angle while the trailing edge is the receding angle. For the latter method, a needle is used to inject or retract fluid slowly until the contact line moves, with the

advancing angle occurring while increasing the volume and the receding angle occurring while decreasing the volume. In these measurements, the sessile drop does not move until the corresponding dynamic contact angle is met, which then becomes stable during movement. Contact angle hysteresis is the difference between the advancing and receding contact angles. The larger the contact angle hysteresis, the less mobile the drop [62], [63]. Although static contact angle is commonly used to characterize wettability or approximate the equilibrium contact angle due to its simplicity, it is an inexact and often unreproducible measure that can stabilize anywhere between the dynamic angles depending the history of the contact line motion while the drop is deposited. This is especially problematic when characterizing surfaces where the contact angle hysteresis is large. Some researchers even argue that it is almost impossible to gain any useful information from a static contact angle [62], [64]–[66].

In a water system, surfaces with an equilibrium contact angle less than 90° are considered hydrophilic. These surfaces have a stronger affinity for water, maximizing its contact area with the surface. On the other hand, surfaces with equilibrium contact angles greater than 90° are considered hydrophobic surfaces. These surfaces repel water and try to minimize the contact area with the liquid. Typically, the maximum angle for a smooth, homogeneous, and hydrophobic surface is between 125-130° [63]. To generalize low- and high-contact angle fluid-surface systems to more than just water, some researchers have begun using the terms hygrophilic and hygrophobic [67] (the prefix hygro- means liquid). Hygrophilic refers to the fluid-surface system with equilibrium contact angles below 90°, while hygrophobic refers to fluid-surface systems with equilibrium contact angles above 90°. The review will use the terminology used in the corresponding literature cited.

Surface roughness has been shown to magnify the underlying wetting properties, with the contact angles of hydrophilic surfaces decreasing and those of hydrophobic surfaces increasing [68]. This understanding was first theorized by Wenzel [68]–[70] and is known as the Wenzel state. For hydrophilic surfaces, roughening can cause the surface to become hemiwicking, also known as superhydrophilic. In this state, the liquid infiltrates the roughness and spreads over the surface via capillary action, with an approximately 0° contact angle. Bico et al. [71] derived a criterion for this hemiwicking phenomenon, which is when the corresponding change in interfacial energy per unit length is negative. For hydrophobic surfaces, in addition to the Wenzel state, roughening can lead to another state known as the Cassie-Baxter state [72]. In the case of

hydrophobic porous surface structures, air can be trapped underneath the drop, causing the droplet to rest on top of the solid-vapor composite instead of flooding the structure as with the Wenzel state. Surfaces in this state are often known as superhydrophobic and are characterized with contact angles higher than possible on smooth surfaces (>150°) and droplets with low roll-off angles due to low contact angle hysteresis [73], [74].

A unique class of hydrophobic surfaces are parahydrophobic surfaces, which refers to surfaces having high advancing contact angles and a very large contact angle hysteresis [75]. This wetting state is the result of a metastable state that is an intermediate of the Wenzel and Cassie-Baxter states, something that may be known as the Cassie-impregnating wetting state. Because of this large hysteresis, even though droplets may have very high static contact angles when placed on these surface, the droplets exhibit a strong apparent adhesion to the surface while minimizing its contact area. This "sticky" wetting behavior is also often called the "petal effect" as it is most commonly associated with the phenomenon on rose petals [76]–[78].

### 2.2.2 Wettability Effects on Boiling

As boiling is a phenomenon that involves a solid, liquid, and vapor, wettability has been shown to have a significant effect on boiling performance and has been explored extensively. Hydrophilic surfaces have been associated with an increase in the critical heat flux even past Zuber's limit due to effective rewetting of the surface after bubble departure [9]–[12]. However, increased wettability is also associated with lower heat transfer coefficients [10], [11]. On the other hand, hydrophobic surfaces have better heat transfer at lower heat fluxes due to the onset of nucleate boiling (ONB) occurring at lower temperatures and higher nucleation densities, but they often reach critical heat flux at very low heat fluxes due to bubble coalescence soon after the onset of nucleate boiling [11], [13], [14]. For this reason, hydrophobic surfaces have not been a primary focus for past boiling investigations.

Superhydrophilic surfaces have been of significant recent interest for boiling applications due to the observed increases in critical heat flux [79]–[83]. Superhydrophilic surfaces have been observed to provide a CHF improvement to values much greater than that predicted by Zuber's model, with a degree of enhancement that corresponds to the ability of the surface to wick liquid volume by capillary action through the surface structure at a high flux, thereby preventing dryout.

Although highly nonwetting or superhydrophobic surfaces have been studied as sites for nucleation enhancement in the context of heterogeneous biphilic surfaces [79], [80], uniformly superhydrophobic surfaces have largely been overlooked due to the premature critical heat flux. For example, Hsu and Chen [84] and Malvasi et al. [85] showed that such surfaces reached CHF immediately upon the onset of nucleate boiling. However, recent work by Allred et al. [15] challenged this traditional notion by demonstrating highly effective boiling on a notionally superhydrophobic surface, which reached a critical heat flux of 115 $W/cm^2$. This was accomplished by boiling a surface from the Wenzel state instead of the Cassie-Baxter state, which caused a pinning of the three-phase contact line. Furthermore, low superheats were observed due to the high nucleation site densities, taking advantage of the favorable nucleation characteristics of hydrophobic surfaces at low heat fluxes. Based on observation that the primary difference between these two wetting states was the dynamic wettability, this study suggested that dynamic wettability was the primary indicator of boiling behavior, rather than static contact angle characterizations. Based on this understanding, highly efficient boiling was demonstration from a parahydrophobic surface, which was able to achieve a higher heat transfer coefficient and similar CHF as a hydrophilic surface tested despite its high static contact angle [16]. This was due to the favorable bubble dynamics of these surfaces, with small, spherical bubbles that easily departed from the surface. This study showed that the receding contact angle in particular was the important wetting attribute that governed growth dynamics and critical heat flux performance, and further work formulated a model to describe maximum base diameter dependent on receding contact angle [17].

### 2.2.3 Numerical Investigations on the Effects of Dynamic Wettability on Boiling

Numerous computational studies have been performed to investigate boiling and the bubble ebullition cycle, which have been reviewed extensively in Ref. [86]. This current literature review will focus on those studies that consider the effects of surface wettability on boiling. One of the first complete simulations of saturated nucleate pool boiling was performance by Son et al. [87]. A finite difference scheme was used to solve governing conservation equations, and a level-set method was used to capture the vapor-liquid interface, which expanded and contracted as the bubble grew and departed. The study quantified how static contact angle and superheat affected the bubble dynamics. Although their study did not consider dynamic contact angles or contact

angle hysteresis, they recognized that they both may influence the shape of the vapor-liquid interface at the heated surface during departure in a real system. Most other computational studies similarly have only used static contact angles.

Mukherjee and Kandlikar [88], [89] explored the effects of dynamic contact angle on single bubbles by numerically solving the complete Navier-Stokes equation and capturing the liquid-vapor interface with the level-set technique. They found that different dynamic contact angles resulted in a stick/slip interface movement during growth and different bubble departure diameters. A larger advancing contact angle was found to increase vapor removal rate. Higher contact angles caused larger departure diameters, which disturbed the thermal boundary layer and increased heat transfer.

Chen et al. [90] studied bubble formation with a moving contact line on orifice plates using a similar process: numerically solving Navier-Stokes and using the level-set method. Although not a direct simulations of boiling heat transfer, the effects of dynamic contact angles on bubble departure size were explored. Using two different models, a contact line velocity dependent model and a stick-slip model, they found that maximum contact diameter increased linearly with departure diameter. Moreover, both the advancing and receding contact angles impacted contact diameter, with larger contact angles corresponding with a larger maximum contact diameter. While advancing contact angle only had a slight influence, the receding contact angle had a strong influence and was identified as the primary factor.

Allred [17] performed numerical studies exploring the effects of dynamic wettability on the bubble ebullition cycle and the corresponding heat transfer mechanisms during bubble growth. Using two-phase continuum surface force volume-of-fluid simulations, a framework for bubble ebullition based on dynamic contact angles was defined: a receding phase where the bubble grows at a constant receding contact angle until the maximum contact diameter is reached, contact line pinning phase where the contact angle increases until the advancing contact angle is reached, and finally an advancing phase where the contact diameter decreases at the constant advancing contact angle and until departure from the surface. This study found that receding contact angle governs the maximum contact diameter, while the advancing angle determines how long it remains in the pinning phase and how the bubble departs—either fully departing or pinching off and leaving a residual bubble. With this understanding, wettability regimes based on dynamic contact angles instead of the traditional static contact angles were defined. Hygrophilic fluid-surface systems are

redefined as those with both receding and advancing contact angles less than 90°. Hygrophobic systems are redefined as those with both receding and advancing contact angles greater than 90°. A third regime, ambiphilic, is defined as a fluid-surface system with a receding contact angle below 90° and an advancing contact angle above 90°. With this definition, the previous parahydrophobic classification is an example of a water-surface ambiphilic system with large contact angle hysteresis.

Within this framework, hygrophilic systems have small contact diameters with small, rapidly departing bubbles that fully rewet. Hygrophobic systems have large contact diameters and depart by pinching off, which minimizes the waiting period at the expense of rapid vapor spreading. Finally, ambiphilic systems had small contact diameters and a pinch-off at departure, taking the advantageous characteristics of both hygrophilic and hygrophobic systems.

Building upon this framework, Allred [17] also numerically explored the heat transfer mechanisms associated with bubble departure across these regimes. This diabatic model considered the heat transfer via conduction, convection, and from the microlayer for the hygrophilic and ambiphilic surfaces. During the receding stage, hygrophilic systems experienced a short-lived, but extremely effective heat transfer due to the microlayer. This short period of highly effective heat transfer was due to the very small microlayer thickness, which lead to small thermal resistance but rapid dryout. During pinning, the microlayer is thicker, causing heat transfer that is a magnitude of order lower, and then becomes comparable to that of convective and conductive heat transfer near the contact line. As the contact line advances, the microlayer heat transfer diminishes while convection and conduction heat transfer increase. Considering the entire process, the contact line heat transfer has the highest proportion of the heat transfer.

Hygrophobic systems do not form a microlayer and most heat transfer occurs at the contact line during the receding and pinned stages. In the receding stage, the temperature remains nearly isothermal with only a slight drop in temperature at the contact line. During the pinning and advancing stage, hot spots form due to the large diameter and vapor formation. The largest heat transfer occurs during the advancing stage due to transient conduction and convective flow.

Ambiphilic systems do not take advantage of the initial thin microlayer growth like the hygrophilic case because pinch-off of the previous departing bubble prevents complete rewetting. This results in lower heat transfer during bubble growth and pinning. Furthermore, conduction near the contact line is minimized due to a small temperature gradient. However, effective heat

transfer occurs during contact line advancement and bubble departure, leading to large local dip in temperature and a peak in heat flux. Although ambiphilic surfaces experience lower microlayer heat transfer, the waiting time is effectively removed, which maintains effective contact-line heat transfer and entirely removes the period of low heat transfer dictated by transient conduction.

These numerical studies have shown that hygrophilic and ambiphilic surfaces have the most potential for effective boiling application. Hydrophilic systems overall have the best per-bubble heat transfer due to effective microlayer evaporation during growth, but the waiting time causes worse nucleation characteristics than ambiphilic. Meanwhile, the ambiphilic system had more favorable nucleation, yet worse heat transfer per bubble when compared with hygrophilic systems. Based on these tradeoffs, and given some of the underlying numerical modeling assumptions, it is hard to discern which wettability regime may ultimately provide the best performance. In particular, previous simulations only consider of the dynamics of a single departing bubble, which fails to capture the effects of nucleation site density and bubble interaction that are present. Furthermore, these findings have not been validated via experiments. It is therefore imperative to experimentally characterize the effects of dynamic wettability on boiling heat transfer.

## 2.3 Infrared Thermography for Pool Boiling

Many experimental tools have been used in the study of nucleate pool boiling. Due to the potential for revealing the mechanism of heat transport at the surface as a function of wettability, this review will focus on the use of infrared thermography to understand boiling heat transfer. Infrared thermography is a technique that uses a sensor to capture the emission of thermal energy from a surface, which is a function of temperature. This technique gives a spatial map of temperature based on the sensor pixel resolution.

Theofanous et al. [46], [91] first developed the infrared thermography approach for pool boiling applications. In their two-part study, a sub-micron Ti heater was deposited on glass and temperature was measured with a high-speed infrared camera from the bottom of the sample. These measurements provided quantitative information on nucleation site density and nucleate boiling heat transfer over a range of heat fluxes up to CHF. These observations were not possible before at high heat fluxes, revealing for the first time the viability of using infrared imaging from the bottom to assess nucleation characteristics of pool boiling.

For infrared investigations of pool boiling, an IR-opaque thin film resistive layer is typically used for heating, such as the sub-micron Ti heater of the prior study. For most of these studies, the resistive layer is submerged, and boiling occurs on an exposed region between two electrodes due to resistive (Joule) heating. The heater must be IR opaque so that the emission corresponds to the temperature of the bottom of the heater. Furthermore, thin film heaters are used so the temperature drop through the film and the heat capacity are negligible. This allows temperatures measured at the bottom of the heater to correspond with the temperature of the boiling surface in contact with the fluid. Although thin metal foils have been used in some IR boiling studies [32], [92]–[95], most studies use an IR-transparent substrate coated with an IR-opaque conductive heater [23], [46], [91], [96]–[104]. Common metals used for heaters are titanium [46], [91] and chromium [96], [97], which are opaque to both visible and infrared light. Another commonly used conductive material used as a heater is indium tin oxide (ITO), which is both IR opaque and visibly transparent, as used in Ref. [98]–[102], [104]. When used in conjunction with a visibly transparent substrate such as sapphire [103] or calcium fluoride [23], [96], [97], [101], [102], simultaneous infrared and high-speed imaging can be taken from the bottom of the heater.

Although most of the studies with IR thermography used IR opaque heaters in contact with the liquid, some studies used heaters not in direct contact with the liquid with a separate IR opaque layer. Kim and Kim [105] used heater design that consisted of an IR-transparent silicon substrate as the heater from the bottom (not in contact with the water), an insulated IR transparent polyimide layer, and a Ti IR opaque layer in contact with water. Jung et al. [100] used a similar design with the exception of the IR opaque layer, which used black paint instead of Ti. Although this setup may have fewer safety concerns as the heater is not in direct contact with liquid, this setup had to account for the additional interfaces and conduction from the heater to the surface.

Using IR thermography and high-speed imaging, information on bubble ebullition and the heat transfer mechanisms can be obtained. Gerardi et al. [98] gathered data on the bubble radius, microlayer radius, dryout radius, and various heat transfer mechanisms, concluding that heat transfer from the re-formation of the thermal boundary layer after bubble departure was the dominant contributor to heat transfer. Jung et al. [100] explored boiling of FC-72 up to CHF, using IR to measure local temperature and heat transfer coefficients. This study found that the liquid-area heat transfer was the predominant heat transfer mechanism at CHF and described the process by which CHF occurs; CHF was related to the wetted area fraction, and a higher CHF could be

achieved by increasing wetted area fraction via methods such as decreasing contact angle. Kim and Kim [105] also explored the heat transfer mechanism during nucleate boiling, concluding that liquid area convection was the predominant heat transfer mechanism, mainly due to it having the largest area fraction.

In addition to infrared thermography and high-speed imaging, researchers have added inspection additional techniques, in particular to observe the microlayer. Laser interferometry has been used to explore the microlayer thickness [106], [107] and total internal reflection-based techniques have been used to explore the liquid-vapor phase distribution [108], [109] on boiling surfaces. Jung and Kim [23], [101], [102] integrated these two techniques with IR thermography and high speed imaging to explore the microlayer geometry and the associated heat transfer mechanisms in a single bubble. In these studies, the heat transfer mechanisms of the microlayer were captured, the complete bubble geometry including the microlayer was obtained, and models were created for the initial microlayer thickness. The same research group also developed a method of detecting the three-phase contact line by simply using infrared thermography and taking advantage of the different IR absorptivity of vapor and water [110]. Duan et al. [99] integrated particle image velocimetry with IR thermometry and high-speed imaging to study the bubble ebullition cycle, temperature history of the surface, and velocity distribution within the liquid.

The use of IR thermography and high-speed flow visualization have also been used to study the effects of surface modifications. Kim et al. [111] studied nucleate boiling from four samples with micro-pillar arrays containing various gaps was studied to explore the effects of microstructure gap on bubble parameters. This was accomplished by measuring temperature via infrared from the bottom and observing bubble growth via a high-speed camera from the side. The study found that the structured surfaces produced larger bubble sizes, lower bubble departure frequency, and lower nucleation site density. Tetreault-Friend [103] used infrared thermography and an ITO heater to explore the effects of hydrophilic coatings on boiling heat transfer and critical heat flux. Surfaces of varying pore layer thickness, pore size, and void fraction were created with hydrophilic $SiO_2$ nanoparticles of various sizes and polymers. CHF improvements up to 114% were reported, and results suggested that CHF depends on capillary pressure and viscous pressure drops. Although IR thermography was used in this study for temperature measurement, the bubble ebullition characteristics were not investigated.

As shown in the literature, IR thermography and high-speed flow visualizations have been used for pool boiling. Moreover, they are effective tools in assessing nucleation phenomenon and heat transfer. However, none of the studies using this technique have explored how dynamic wettability affects the nucleation characteristics, which has been shown to have a strong impact on boiling heat transfer.

# 3. METHODOLOGY

To experimentally characterize how dynamic wettability affects bubble ebullition and boiling heat transfer, water is boiled from thin film heaters having coatings that engender wetting characteristics of the three proposed regimes: hygrophilic ($\theta_{rec}$, $\theta_{adv}$ < 90°), hygrophobic ($\theta_{rec}$, $\theta_{adv}$ > 90°), and ambiphilic ($\theta_{rec}$ < 90, $\theta_{adv}$ > 90°). The thin film heaters were fabricated on silicon (Si) wafers with titanium (Ti) as the resistive layer and silver (Ag) for the electrical contacts. Si was chosen as the substrate because it is sufficiently IR transparent, with an approximately constant transmittance of 54% between the IR lens range of 3 and 5 μm [112] and readily processed using standard microfabrication techniques. Furthermore, although Si partially absorbs and emits within the IR lens range between 3 and 5 μm, the absorption coefficient is not strongly dependent on temperature or wavelength as other potential substrates such as sapphire [113], therefore easing the calibration process. The Ti layer was used because no additional steps are required to achieve a wetting behavior representative of the hygrophilic regime when used with water. Furthermore, Ti is IR opaque, allowing for the direct measurement of the surface temperature at this layer. To achieve the wetting characteristics of hygrophobic and ambiphilic systems, the thin film heaters were coated with Teflon and polydimethylsiloxane (PDMS), respectively. Section 3.1 discusses the fabrication process.

These samples sealed into a pool boiling facility that measures the spatiotemporal surface temperature distribution from below via high-speed infrared thermography and captures the bubble ebullition characteristics from the side via high-speed flow visualization. The facility controls and monitors both the temperature and pressure of the pool for the entirety of the experiment. Section 3.2 discusses the pool boiling facility. Section 3.3 discusses information on the IR camera and calibration procedure. Section 3.4 discusses the experimental procedure and data processing.

## 3.1 Surface Fabrication and Characterization

To create the thin film heaters, a Si wafer undergoes cleaning; two lift-off processes that involve photoresist coating, metal deposition, and photoresist removal; dicing to get the proper dimensions; and an additional coating if needed to achieve the specific wetting characteristics.

The dimensions of the thin film heater are shown in Fig. 3.1 The heater portion, which is the surface boiling occurs, is the 2 cm × 2 cm region of exposed Ti between the two Ag electrodes.

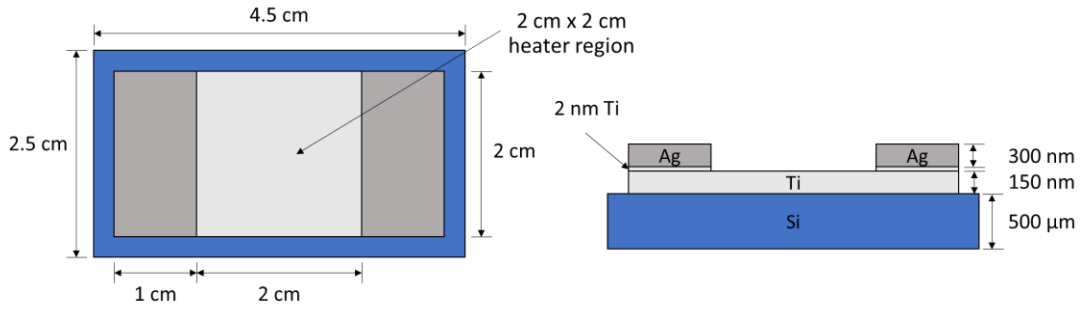


Figure 3.1. Schematic diagram of the thin film heater with a Si substrate, Ti resistive layer, and Ag electrode. Boiling occurs on the exposed 2 cm x 2 cm Ti heater region.

The thin film heaters are fabricated on 100 mm diameter Si wafers with 300 nm $SiO_2$ (University Wafer, P type, B dopant, [100] orientation, SSP, Test Grade). The wafers are first cleaned by a 5 min sonication each in toluene, isopropyl alcohol, and acetone. Further cleaning is accomplished by soaking in a Piranha solution (3:1 volume ratio of $H_2SO_4$ and $H_2O_2$) for 8 min, rinsing with deionized water, drying with $N_2$, and a baking on a hot plate for 5 min at 120 °C to remove residual moisture.

After cleaning, a photoresist lift-off and deposition process is used to form the desired rectangular dimensions of the thin film heater. The wafer is first primed with hexamethyldisilazane (HMDS), an adhesion enhancer, and coated with AZ1518 photoresist via spin coating at 4000 rpm. The wafer is then baked at 100 °C for 2 min on a hot plate to cure the photoresist. Using a photomask (Fine Line Imaging) and mask aligner (Suss, MA 6 Mask Aligner), the sample is exposed for 8 sec and developed with MF-26A for 60 sec. The wafers were then rinsed with deionized water, dried with $N_2$, and heated for 2 min at 100 °C to remove residual moisture. A 150 nm thick layer of Ti is deposited over top of the developed photoresist using e-beam evaporation (CHA Industries, Telemark Model 861 Deposition Controller). Following Ti deposition, the residual photoresist is removed by soaking in acetone for 24 hr, completing the first lift-off process and forming rectangular regions of Ti to serve as the resistive element of the thin film heater.

A second lift-off and deposition process follows the same steps to form the Ag electrical contact pads, with the exception of the pre-cleaning, which only consists of a 5 min soak in toluene,

isopropyl alcohol, and acetone without sonication to avoid damage to the deposited Ti heater layer. For the second lift-off process, 2 nm of Ti and then 300 nm of Ag are deposited, where the Ti is an adhesion layer. After deposition, the wafer undergoes another 24 hr soak in acetone to remove the residual photoresist to complete the process. The sample is then diced to the appropriate size for affixing into the boiling facility.

The heater surface wettability is modified to achieve the desired wetting behaviors by coating the diced heater surface with Teflon or polydimethylsiloxane (PDMS). Prior to coating, the surfaces are prepared to ensure that only the exposed top surface of the Ti heater is coated. This is accomplished by covering the bottom of the sample with Kapton tape and coating the electrodes with AZ1518.

The Teflon coating is created by soaking the samples in a 1% wt/wt solution of Teflon powder and FC-77 (3M, Flourinert). In a beaker, 1.36 g of Teflon powder is dissolved in 80 mL of FC-77 and magnetically stirred for 24 hrs. The prepared sample is then completely immersed in the solution for 30 s and removed. Any excess liquid is shaken off, and the coated sample is cured in an oven at 150 °C for 2 hrs.

The PDMS coating is created by priming the surface and spin coating a diluted solution onto the sample. To create the PDMS solution (Dow Corning, Sylgard 184), a 10:1 ratio of base to curing agent is diluted in hexane. For the sample used in the study, 2.69 g of the base and 0.27 g of the curing agent were weighed in a beaker. These are then combined with 80 mL of hexane, which is subsequently stirred magnetically for 1 hr. Meanwhile, an adhesion promoting primer (DOWSIL, 92-023) is applied completely over the surface via a dropper and spin coated at 500 rpm. The primer then cures at room temperature for 30 min. After the primer cured and the PDMS solution fully dissolved, the PDMS solution is dropped onto the surface and spin coated at 500 rpm. The sample is then left at room temperature for 1 hr and cured in an oven at 150 °C for 30 min.

Following the curing of the Teflon or PDMS, the Kapton tape and AZ1518 were removed. The photoresist was removed by placing the sample upright in a beaker filled with enough acetone to cover the electrode for ~ 1 hr. After the soak, the residual photoresist was removed by gently wiping it away with a clean wipe also soaked in acetone.

The resulting dynamic contact angles were measured using a goniometer (ramé-hart, 290-F1). A 5 μL drop of deionized water is first gently deposited onto the surface. Using a syringe tip

(32-gauge dispensing tip, 0.260 mm outer diameter, 0.100 mm inner diameter) inserted into the center of the droplet, liquid is added or removed in 0.25 μL increments until a steady advancing or receding contact angle is observed.

## 3.2 Boiling Facility

The experimental facility was designed to perform boiling experiments in a sealed environment that allows for the flow visualization from the front through a transparent viewing window, infrared imaging from the bottom, and continual measurements of pool temperature and pressure. A diagram of the facility is shown in Fig. 3.2, and an image is shown in Fig. 3.3. The walls of the boiling facility were made of polyether ether ketone (PEEK), which has a low thermal conductivity (0.25 W/mK) and good durability at high temperatures. The facility also has two borosilicate glass windows in the front and back to allow for the visualization and lighting. The facility has two condensers that are cooled by circulating water via a pump (Iwaki, MD-30RZ-115NL) and a fan heat exchanger. The first condenser is the Graham condenser, which is used to purge non-condensables from the working fluid prior to the experiment. The second condenser is a coiled copper tube condenser inside the facility, and this is used to condense vapor during sealed operation of the facility.

During the test, pressure is measured with a pressure transducer (Omegadyne, PX409) and temperature with six pool thermocouples (Omega, 1/16", T-type, ungrounded), which are captured by a data acquisition unit (Agilent 34970A) at 1 Hz. The pool thermocouples are referenced to a physical ice-point junction in an isothermal dry block (Fluke, 9101). The pool is boiled continually with immersion heaters to maintain the fluid at saturation temperature (Hotwatt, 170W, 1/4" D, 5" L). Pressure is controlled with a proportional-integral-derivative (PID) solenoid valve (Aalborg Instruments, PSV-5). The pool heaters and PID valve were powered by power supplies (Sorensen XG 150-5.6, BK Precision, 1786B). To keep the temperature and pressure constant in the facility, the PID valve took information from the pressure transducer and altered the rate at which water was condensed back into the pool via the coiled condenser.

The sample is attached to the facility via a removable, cylindrical PEEK sample holder, which is screwed onto the bottom of the facility and sealed with an O-ring (McMaster-Carr 1289N244). The removable sample holder is shown in Fig. 3.2(c). The sample holder has a tunnel under the heater portion of the sample to allow for infrared imaging. The sample was sealed onto

the holder by placing a bead of silicone RTV (Momentive, RTV 106) around the tunnel. Once the RTV cures, a smooth bead of epoxy (3M, DP110) is applied across the front and back edges. This smooth coating helps to minimize bubble nucleation from the sharp edges of the sample. After the epoxy cures, the top of the sample holder is screwed on, which contains a total of ten spring loaded electrical contacts (Mill-Max, 0868-0-15-20-82-14-11-0) that connect supply wires to the exposed Ag contact pads of the thin film heater. The wires fed through holes on the sample holder to the power supply (Ametek, XFR 150-18), and the wire holes are sealed with epoxy on the bottom of the sample holder. To minimize exposure of the electrical contacts with the water, they were encapsulated with an epoxy potting compound (3M, DP270).

A right-angle mirror mount (Thorlabs, KCB2C) with an IR-reflective gold mirror (Thorlabs, PF20-03-M02) is screwed onto the bottom of the sample holder via 60 mm cage mounts. The IR image is reflected by the mirror to the IR camera (FLIR, SC 7500), which used a midwave IR 25 mm lens (Janos Technology, ASIO 25 mm F/2.3 MWIR, Model 40494-0393). The lens has a wavelength range from 3-5 μm. To minimize IR noise by blocking potential interferences from the surroundings, the cage mount was completely wrapped in black cloth, forming an enclosed tunnel from the sample to the IR camera. This camera was controlled using ResearchIR, a thermal analysis software by FLIR. Information on the IR temperature calibration procedure is included in Section 3.4.

Flow visualization through the front window is taken using a high-speed camera (Phantom, VEO 710L) and a macro lens (Zeiss, Makro-Planar T* 2/100). This camera was controlled using Phantom Camera Control, the manufacturer's software. The visualizations are back-lit with uniform high-intensity lighting (Advanced Illumination, BT200100) through the back window and additional front-lighting (Sunoptics, Titan300).

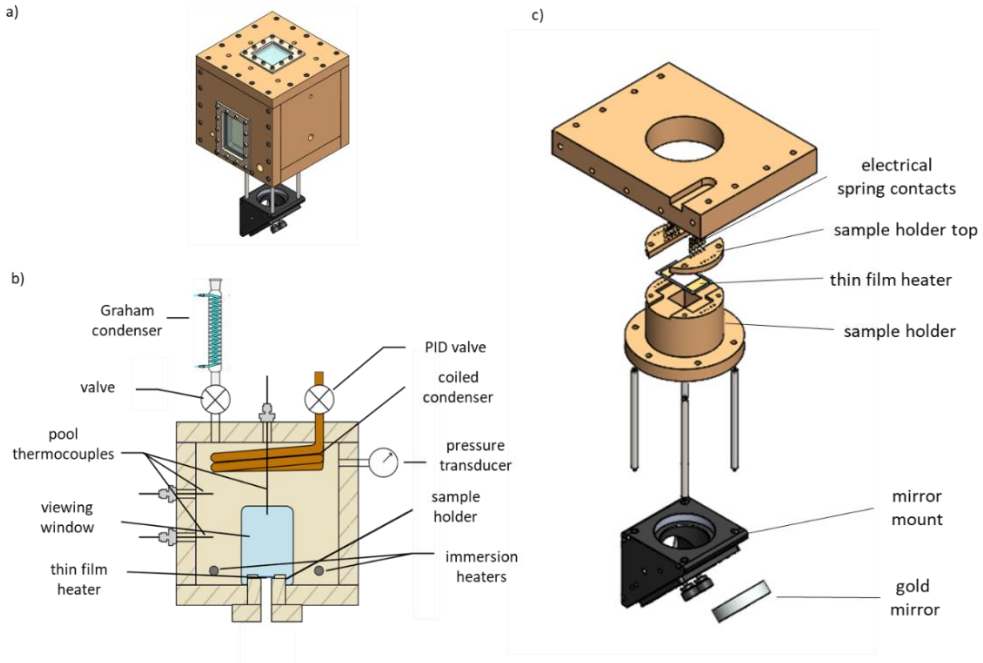


Figure 3.2. (a) Diagram of the pool boiling facility. (b) Cut-out view with labels. (c) Exploded view of the sample holder with labels.

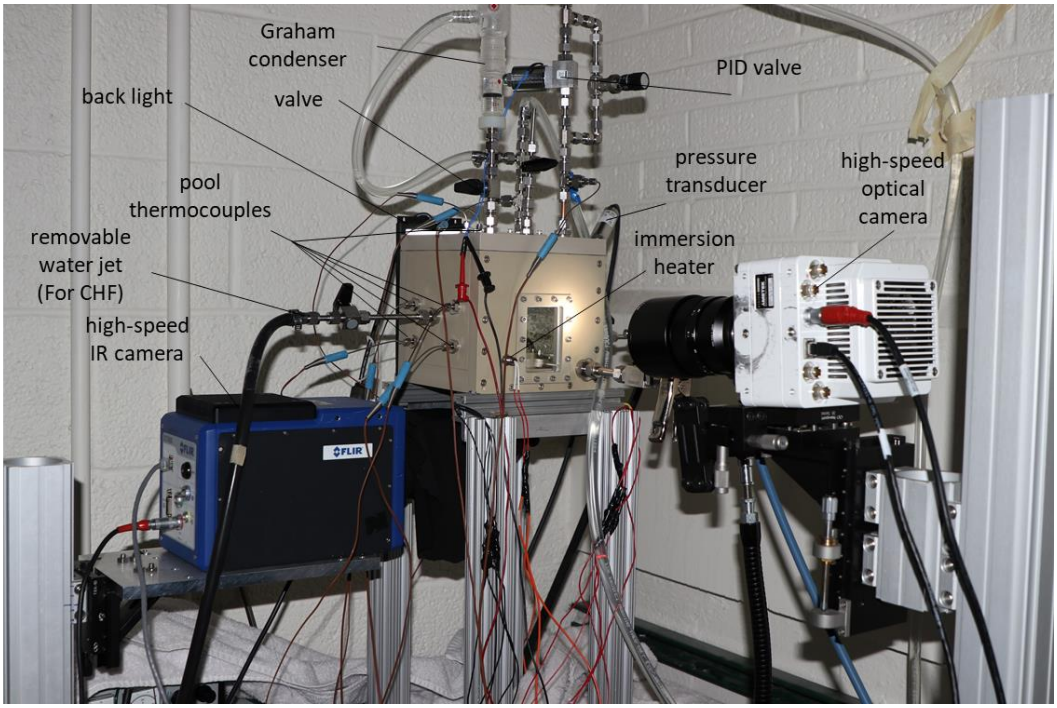


Figure 3.3. Image of the pool boiling facility.

## 3.3 Infrared Calibration

The infrared camera was calibrated by recording digital levels from a black body at known temperatures from 87.5 °C to 135 °C, and then fitting a polynomial of the digital levels of each pixel to the setpoint temperature. A custom-made black body calibrator was built by using cartridge heaters to control the temperature a black-painted copper block as measured with a thermocouple and then viewed by the camera. The camera integration time was set to 45 μs and the framerate was set to 1250 Hz (the same rate as used in the experiments). At each temperature, 3750 frames were recorded and averaged, which was used for the pixel-by-pixel calibration. An algorithm fits the digital levels to temperature with a fourth-order polynomial for each pixel. An example calibration curve for one pixel is shown in Fig. 3.4. Using the polynomial, the algorithm converts recorded digital levels at each pixel across the frame to a temperature.

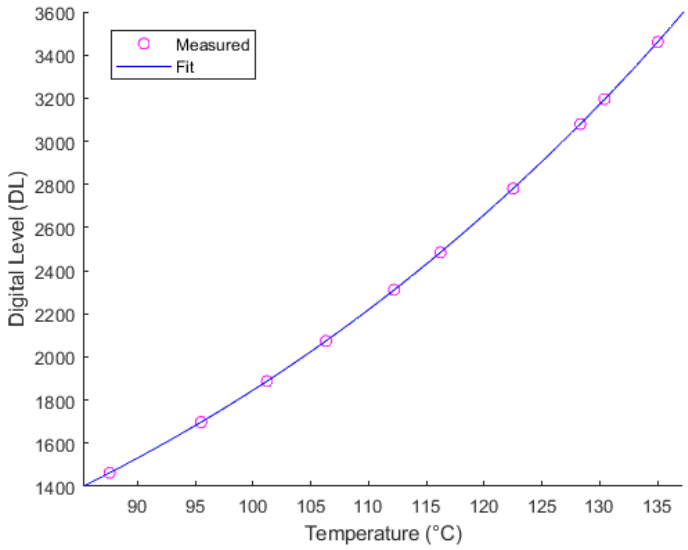


Figure 3.4. Example of a fourth-order polynomial fit for one pixel to correspond digital level to temperature.

When recording, the infrared camera performs a non-uniformity correction to account for detector drift. This accounts for interference from heat generated from the infrared camera by measuring radiation from its own optics and adjusting the gain of each pixel accordingly. This occurs automatically within the camera without user input.

When viewing the bottom of the sample substrates in the pool boiling facility, the irradiation measured by the detector is not strictly equal to the emission from the surface of interest. To account for factors such as absorption and reflection from the substrate and imperfect reflection from the gold mirror, an in-situ correction was performed by corresponding the recorded IR temperature to a known value. Prior to the experiment and after degassing, the pool was allowed to boil for an additional 20 min via the immersion heaters to ensure that steady-state temperature was reached. During this process, no power was provided to the thin film heater. Due to the small thickness of the IR opaque layer, the temperature of the bottom of the Ti layer was assumed to be that of the pool. An average pool temperature was measured with six thermocouples over a period of 50 seconds. While the temperature of the pool was recorded via these thermocouples, the IR camera recorded 3750 frames (3 sec) of the bottom of the sample. A correction factor was calculated for each pixel to account for the difference between the pool temperature recorded by the thermocouples and that recorded by the infrared camera, and this correction factor was applied to the rest of the temperature measurements for the remainder of the experiment. This factor was similar between tests, but to ensure accuracy, a new correction factor was calculated for each corresponding test. Although there are limitations to this in-situ correction, this approach was taken because of its simplicity and the fact that silicon does not have an absorptivity that is affected strongly by wavelength or temperature, and transmittance for the wavelengths of interest between 3-5 μm was constant. Therefore, these factors that affect the infrared measurement are constant, suggesting this in-situ correction is adequate.

### 3.4 Experimental Procedure

After fabrication of the thin film heaters and contact angle characterization, the samples are sealed and tested in the pool boiling facility. Prior to each test, the pool boiling facility is cleaned with IPA to remove any potential contaminants. Also, resistance of each electrical component involved—including each wire, fuse, spring connection, bus bar, and the thin film heater itself—is measured before and after each test using an ohm meter. Once the top portion of the sample holder is attached and the sample holder is sealed into the facility, deionized water is poured to fill the chamber approximately 1 cm above the viewing window. At this point, data collection that measured the temperature and pressure every second begins. The pool immersion heaters are turned to 120 V to bring the water to saturation temperature and to begin the degassing process.

The top of the pool boiling facility is then attached, and every valve is closed except for the Graham condenser. The cooling pump and heat exchanger are then turned on to condense vapor coming through the Graham condenser while allowing noncondensables to purge from the chamber. Once the pool reached the saturation temperature and there were no visible air bubbles, the pool was boiled for an additional hour prior to the test. Following the degassing, the Graham condenser was sealed, and the PID valve is set to maintain the chamber pressure at 101 kPa.

The IR and visual cameras are then set up. The IR focal length was kept constant, and the image was focused via a translation stage attached to the IR camera and centered via the mirror mount. A removable target underneath the sample was used to achieve the focus. The IR camera was set to record at 1250 Hz with a 45 μs integration time at a resolution of 160 × 128 pixels. To ensure repeatability of the measurements, the same sample viewing region and pixels on the sensor were used for each test. The visual camera is centered on the viewing window and focused to the center of the surface, and the framerate was set at 1500 Hz. The aperture, exposure time, and exposure index were changed in conjunction with the front and back lighting.

During the experiment, the voltage to the thin film heaters was increased in predetermined intervals and allowed to boil for at least 15 min to reach steady state. At each set point, footage was taken with both the IR and visual cameras. A wide variety of measurement and metrics can be taken and calculated, as summarized in Table 3.1.

Table 3.1. Information gathered from the experiment and the tools used.

| **Information Gathered** | **Tool Used** |
|---|---|
| Contact line mechanics | Visual |
| Boiling curve: q'' vs superheat | IR |
| Boiling curve: h vs q'' | IR |
| Total ebullition time | IR |
| Temperature Distributions | IR |
| Nucleation Site Density | IR |

To characterize the bubble ebullition, the high-speed visualizations is used. A single characteristic bubble is identified, and the entire ebullition cycle is observed frame-by-frame. To

formulate the boiling curve, the heat flux is calculated by dividing the input electrical power, which is calculated by multiplying the voltage and current, by the heater area. The superheat was calculated by subtracting the saturation temperature at the chamber pressure from the mean temperature at a given heat flux. The mean temperature is taken as the average of the 3750 frames recorded across the entire surface. The heat transfer coefficient is calculated by dividing the heat flux by the mean superheat. The nucleation time is calculated by observing the IR data frame-by-frame and recording the frame at which a distinguishing feature of the ebullition cycle occurred periodically. Taking an average across multiple ebullition cycles, an average ebullition time is calculated. Finally, the nucleation site density is calculated by playing the IR video frame-by-frame, manually notating each nucleation site, and dividing by the area of observation.

# 4. RESULTS AND DISCUSSION

The goal of this study is to experimentally characterizes the bubble ebullition and boiling performance of surfaces with differing dynamic wettabilities spanning the three characteristic regimes of wettability. In particular, the key attributes of the contact line mechanics and overall boiling performance were compared with surfaces that were characterized in each of the three regimes in a system that uses deionized water. From these observations, explanations for the relative improvements in performance were related to the observed bubble dynamics, which included the maximum contact diameter, ebullition time, and nucleation site density.

Three thin film heaters with exposed Ti, Teflon, or PDMS surfaces were fabricated with the procedures discussed in Section 3.2. Using a goniometer, the dynamic wettabilities of these surfaces were characterized as shown in Fig. 4.1.

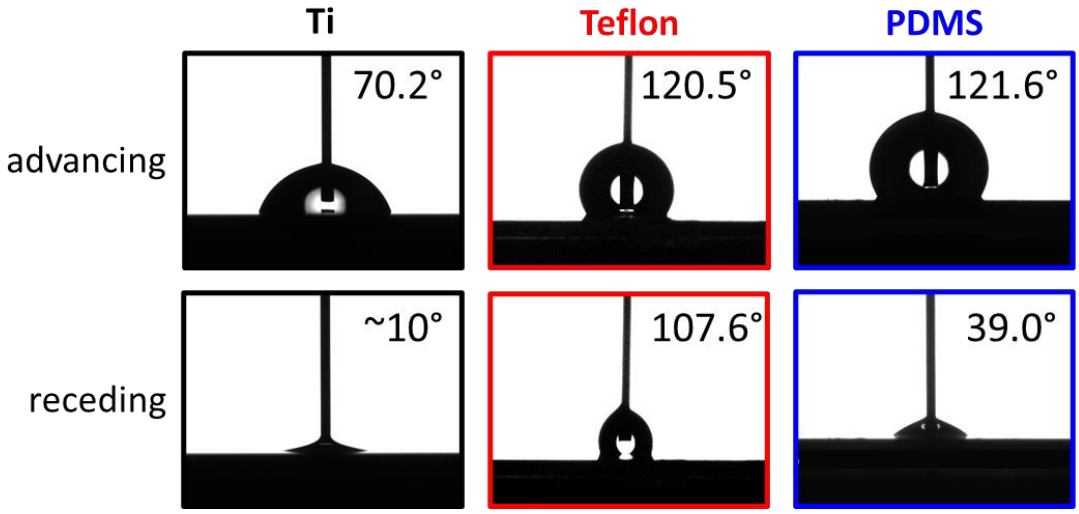


Figure 4.1. Measured wettabilities of the Ti (hygrophilic), Teflon-coated (hygrophobic), and PDMS-coated (ambiphilic) surfaces.

With water, the bare Ti surface had an advancing contact angle of 70.2° and a receding contact angle of ~10°, which are both less than 90°. This classifies the Ti surface with water into the hygrophilic regime. The Teflon-coated surface had an advancing contact angle of 120.5° and a receding contact angle of 107.6° with water, which are both greater than 90°. This classifies this PDMS-water system into the hygrophobic regime. The PDMS-coated surface had an advancing contact angle of 121.6° and a receding contact angle of 39.0° with water. Because the advancing

contact angle was greater than 90° and the receding contact angle was less than 90°, this system was classified into the ambiphilic regime. It is important to note that although these surfaces were classified in their respective wettability regimes based on measurements with water; these surfaces would have different contact angles with other fluids. For example, one cannot claim that Ti is a hygrophilic surface or generalize all Ti surfaces as hygrophilic; instead, the Ti surface tested in particular was classified as hygrophilic when used with water.

Using the high-speed visual camera, the bubble ebullition cycle was observed to gain information about the key characteristics of each boiling wettability regime. Fig 4.2. shows the bubble ebullition cycle for the three surfaces. By looking at each frame, the contact line behavior can be observed, namely the nucleation, receding, pinning, advancing, and departure of the bubble. During the receding stage, the bubble grows with a constant contact angle at the receding angle. Once the bubble reaches the maximum diameter, it the contact line pins and has no motion. During this pinning stage, the contact angle increases until it reached the advancing contact angle. Once the advancing angle is reached, the contact line begins to move inwards as water advances towards the center until departure.

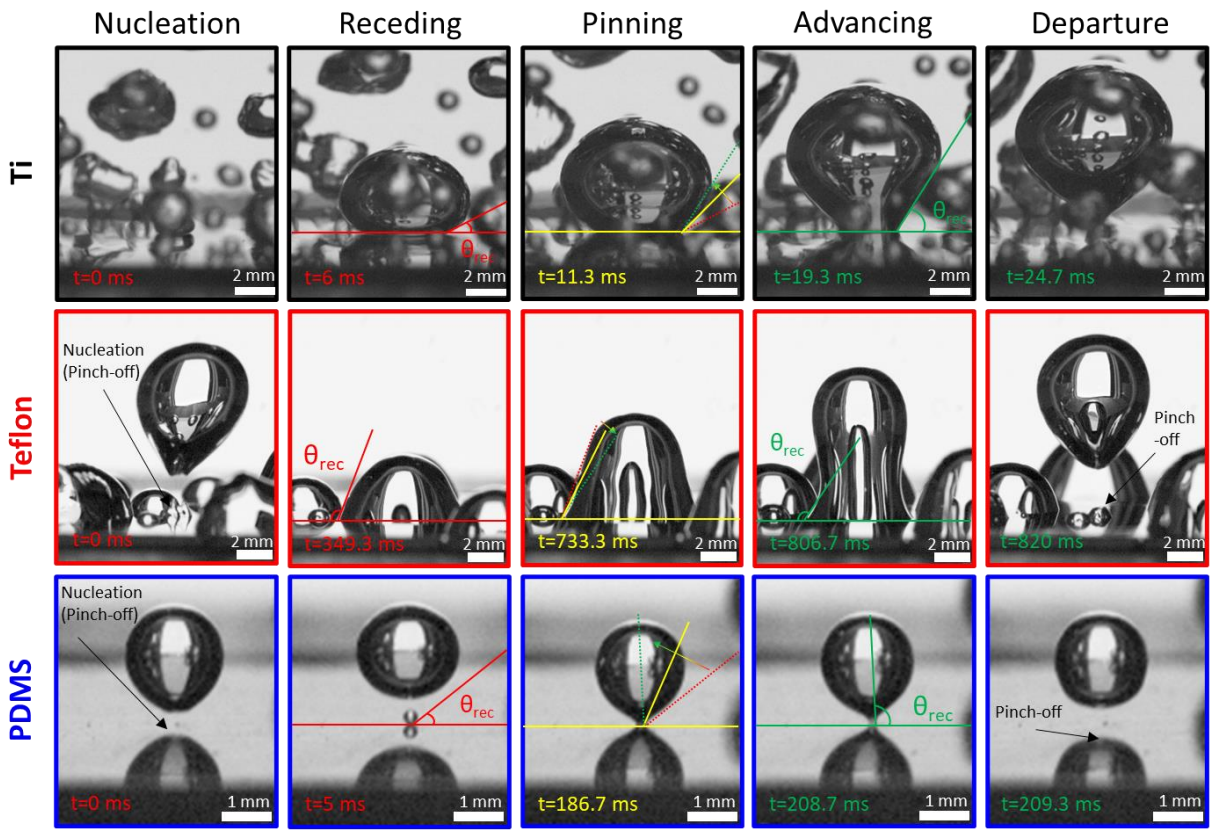


Figure 4.2. Nucleation, receding, pinning, advancing, and departure for the Ti, Teflon, and PDMS surfaces. The heat fluxes were 8.5 W/cm$^2$, 1.0 W/cm$^2$, and 1.1 W/cm$^2$, respectively.

For the Ti surface, the bubble fully departs, and liquid rewets the surface before the next bubble is formed. Even without the temperature data, some basic conclusions can be inferred from the images. From previous studies [11], [17], the general understanding is that the heat transfer that occurs during the waiting time is much less effective than heat transfer during the ebullition process. However, this is also the mechanism that allows wetting surfaces to prevent vapor coverage. Meanwhile, for the Teflon and PDMS surfaces, we can observe a "pinch-off" of the bubble that acts as a seed for growth of the next bubble. With this phenomenon, these surfaces have a minimized waiting time between each bubble. A shorter waiting time allows more effective heat transfer to occur during the formation and departure of a bubble.

Other observations can be made on the relative sizes of the bubble and growth times. The Ti surface had intermediate bubble sizes that were between those of the Teflon and PDMS surfaces. The bubble growth time from nucleation to departure was the shortest at 24.7 ms for the Ti surface. Meanwhile, the Teflon surface had the largest bubble size and significant vapor coverage even at

a low heat flux. As the bubble grew, it coalesced with neighboring bubbles, further exacerbating the vapor coverage. These bubbles also remained on the surface the longest from nucleation to departure at 820 ms. The PDMS surface had very small contact with the surface and experienced a very long pinning stage followed by a very short advancing stage prior to departure. The time from nucleation to departure was 209.3 ms.

The boiling curves for the three surfaces were calculated and shown in Fig. 4.3. Fig. 4.3 (a) shows the heat flux as a function of mean superheat, while Fig. 4.3 (b) shows the mean heat transfer coefficient as a function of the heat flux. Note that the Ti and PDMS surfaces in the data shown here to not extend up to CHF, to avoid damage to the thin-film heater by dryout at high heat fluxes. Instead, the primary focus of the discussion that follows is on the temperature and heat transfer coefficient. However, note that separate boiling tests were performed up to CHF, causing catastrophic failure of the surfaces, to confirm that both the Ti and PDMS surfaces had similar dryout values of ~ 80 W/cm$^2$.

The PDMS surface performed the best of the three tested, as signified by the lowest superheats and the highest heat transfer coefficients for each given heat flux. The Teflon surface performed well at low heat fluxes, but due to an early onset of critical heat flux at 11 W/cm$^2$, the surface temperature dramatically increased, and the heat transfer coefficient decreased. This demonstrates the primary drawback of hygrophobic surfaces and suggests they are not suitable for boiling applications. The Ti surface had the worst performance at low heat fluxes, as indicated by the largest superheats and lowest heat transfer coefficients. However, the Ti surface outperformed the Teflon surfaces at higher heat fluxes because it does not reach CHF at a low heat flux.

Fig. 4.4, Fig. 4.6, and Fig. 4.7 show the temperature profiles and corresponding high-speed visualization images for the Ti, Teflon, and PDMS surfaces, respectively, at several selected heat fluxes. The temperature profiles and images provide insight into the mechanisms leading to the performance differences between the surface. As heat flux increases, the number of bubble nucleation sites for all three surfaces increased. These sites of bubble growth and departure are associated with a drop in temperature for the Ti and PDMS surfaces. However, for the Teflon surface, the nucleation site was indicated by an increase in temperature due to the dry spots forming underneath the bubble, which prevents effective heat transfer from occurring. This adds more evidence confirming the mechanism of early critical heat flux the Teflon surface.

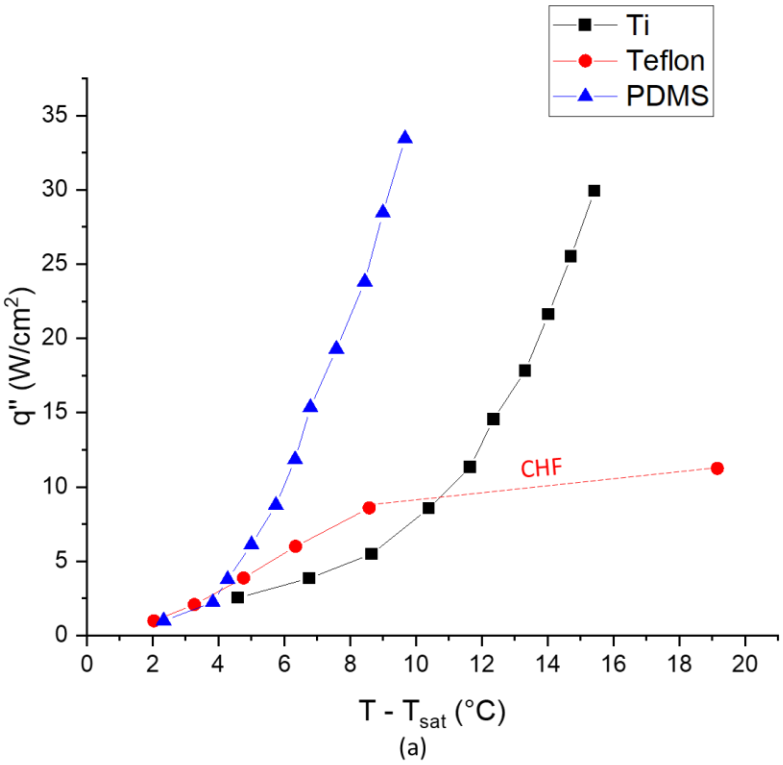


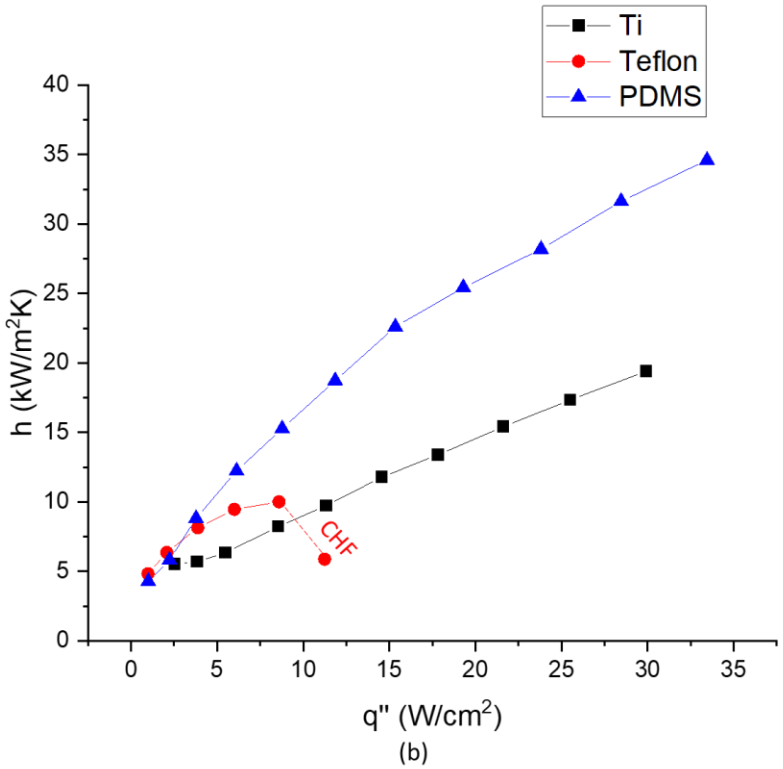


Figure 4.3. Boiling curves with (a) heat flux vs. superheat and (b) heat transfer coefficient vs. heat flux for a Ti, Teflon, and PDMS surface

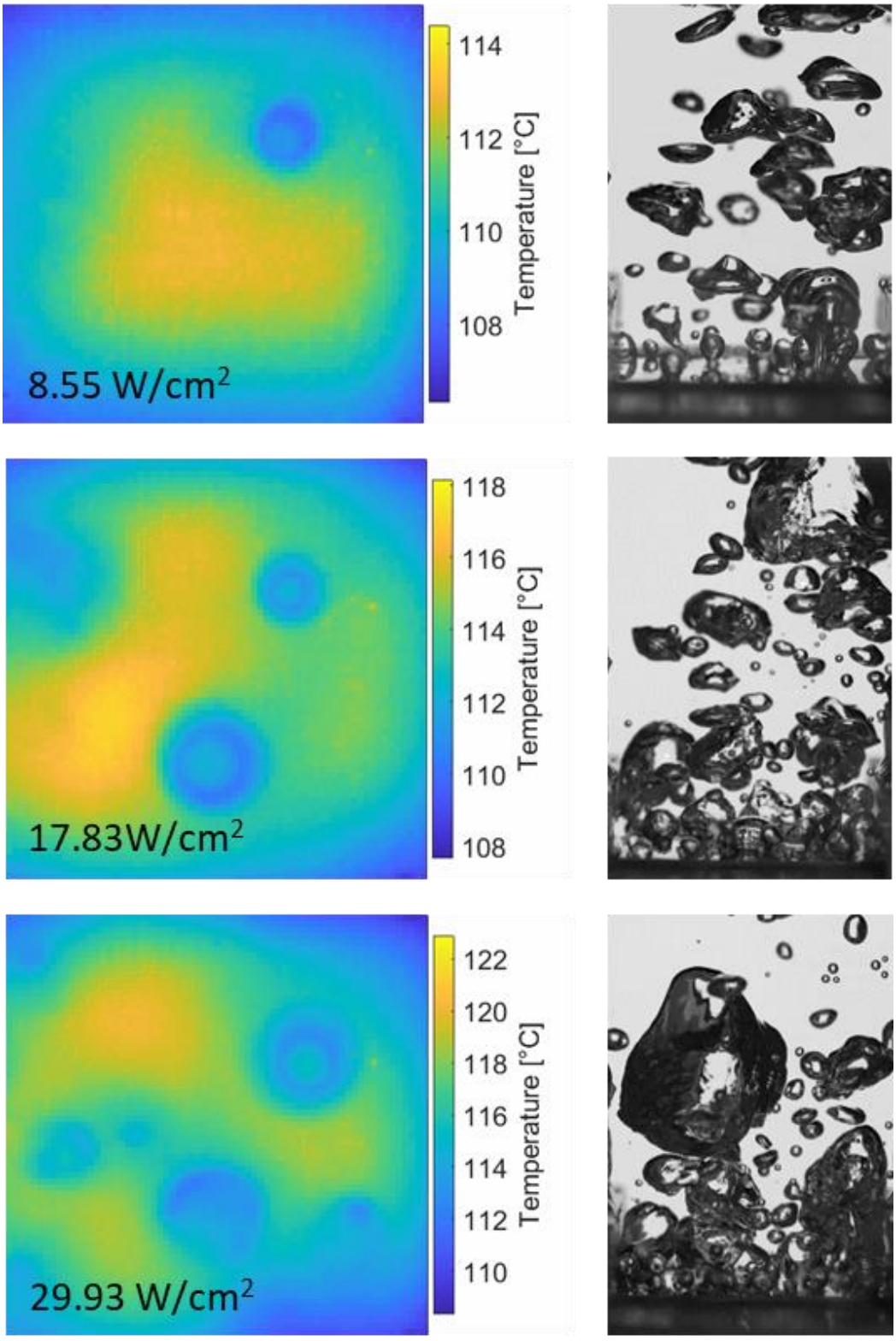


Figure 4.4. Temperature maps (left) and visualization (right) of Ti surface.

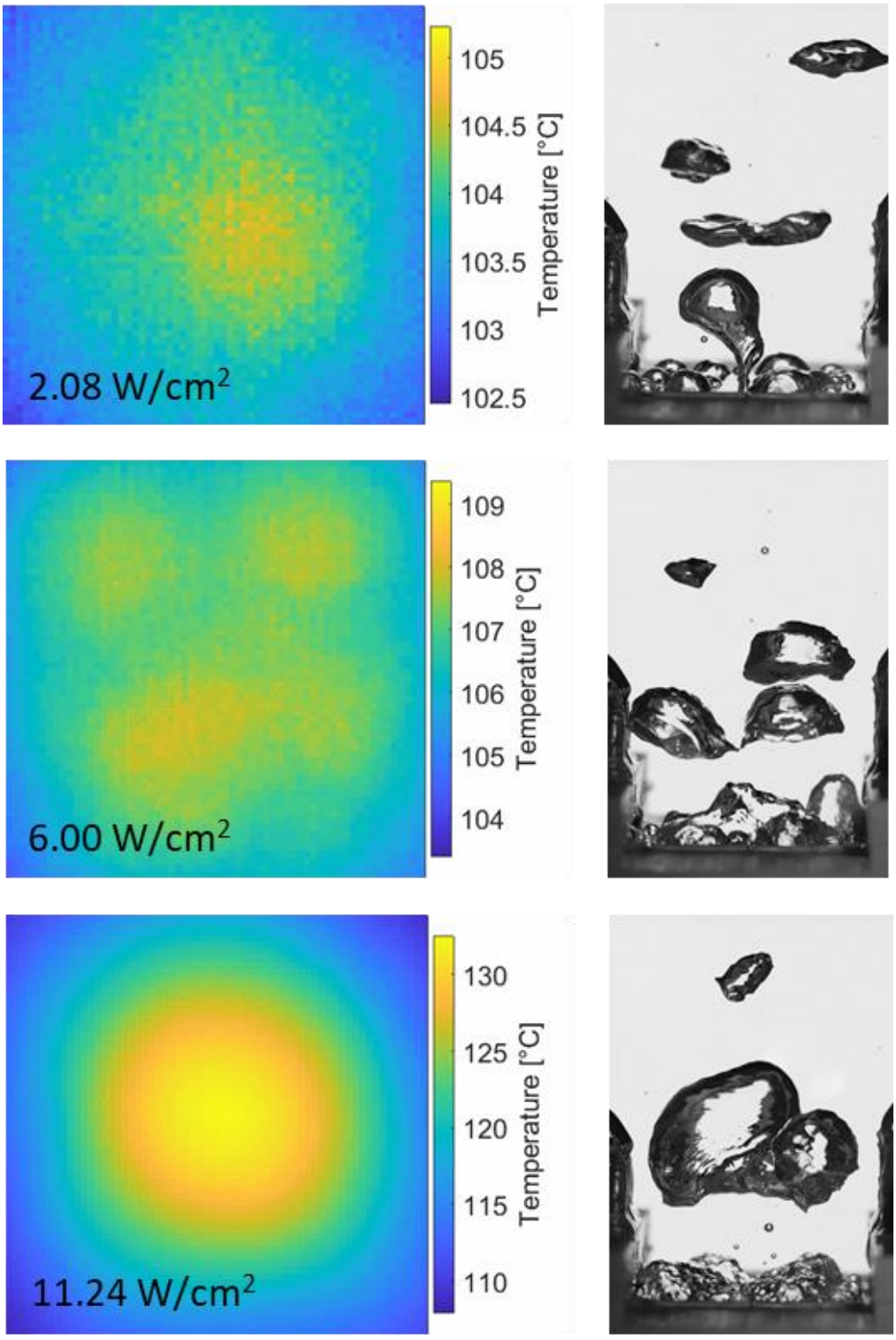


Figure 4.5. Temperature maps (left) and visualization (right) of Teflon surface.

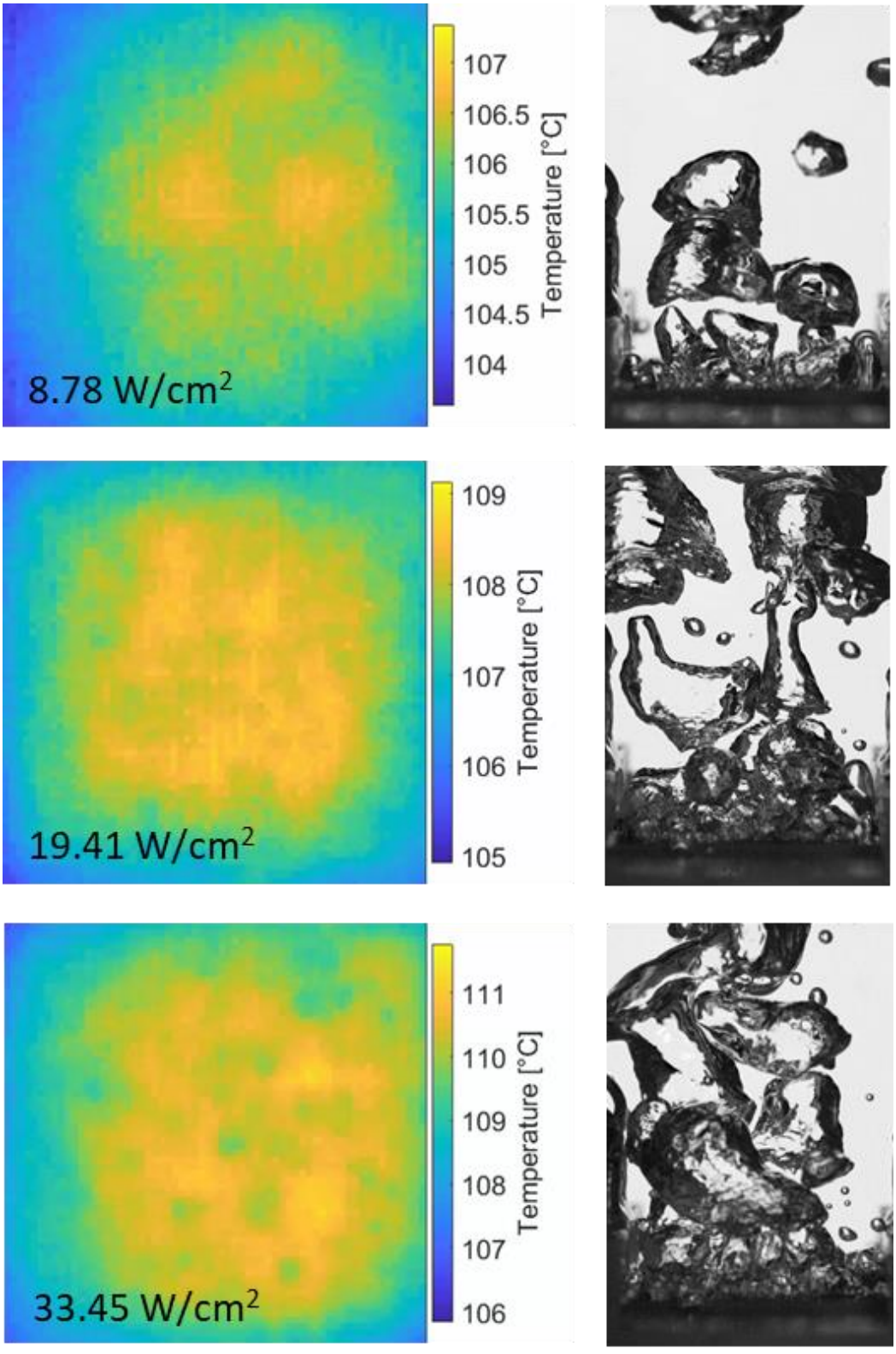


Figure 4.6. Temperature maps (left) and visualization (right) of PDMS surface.

For the Ti surface, as the bubbles grew, the largest drop in temperature occurs at the contact line, suggesting effective heat transfer in this region. Of the three surfaces, the Ti surface saw the largest decrease in temperature compared with the surrounding surface area for a given bubble. Furthermore, regions where bubbles grow are substantially cooler on average than regions areas without nucleation. Although the heat transfer for a single bubble was large for the Ti surface as indicated by the large decrease in temperature, the overall performance of these surfaces is limited by the long waiting times.

For the Teflon surface, bubbles were able to form readily on the surface, even at low heat fluxes. This allowed overall surface temperatures to remain lower than the Ti surface at these lower heat fluxes. However, as shown from the flow visualizations, the bubbles covered a large portion of the surface and coalesced even at lower heat fluxes, leading to the early onset of CHF. Furthermore, because of the larger contact diameters, vapor spreading, and bubble departure that did not allow the surface to fully rewet, the bubbles were characterized as hot spots, as shown from the increase in temperature under the bubbles. This was different from the Ti surface, which saw significant decreases in temperature under the bubble. These hot spots grew to the maximum contact diameter, and departure was characterized by a decrease in temperature as the as the surface partially rewets. Once CHF was reached, the surface was permanently blanketed with vapor, and the temperature increased drastically, with the hottest region occurring in the center.

The results of the PDMS surface were the most intriguing of the three surfaces. At the higher heat flux, although the visualizations show a dense plume of vapor above the PDMS surface that is similar to the Ti surface, the surface temperature maps are able to reveal extreme difference in the nucleation characteristics. The PDMS surface offer an extremely high relative nucleation site density, a rapid ebullition cycle, and very small contact diameters that lead to the enhanced performance of the PDMS surface. The use of infrared thermography to investigate this regime of surface wettability during boiling offer observations and insights that are not possible simply by using side-view flow visualization. With a dense nucleation site density and short ebullition time, more of the PDMS surface undergoes the effective heat transfer that occurs with bubble formation at any given time. Furthermore, the small contact diameters indicate contact line pinning, which prevents vapor coverage that leads to critical heat flux. Because these are the mechanisms that were postulated to have led to the improvement, these parameters were measured to provide a quantitative comparison for the three surfaces.

Fig. 4.7 shows the nucleation site density at a given superheat for the three surfaces. As shown from this plot, the nucleation site density of the PDMS surface was an order of magnitude greater than that of the other surfaces, ranging from $10^5$ to $10^6$ nucleation sites per square meter versus the $10^4$ to $10^5$ nucleation sites per square meter observed for the other two surfaces. This was likely a primary mode of boiling improvement, as the evaporation that occurs during bubble formation has a strong impact on the overall heat transfer performance, especially for wetting surfaces that have a low advancing contact angle.

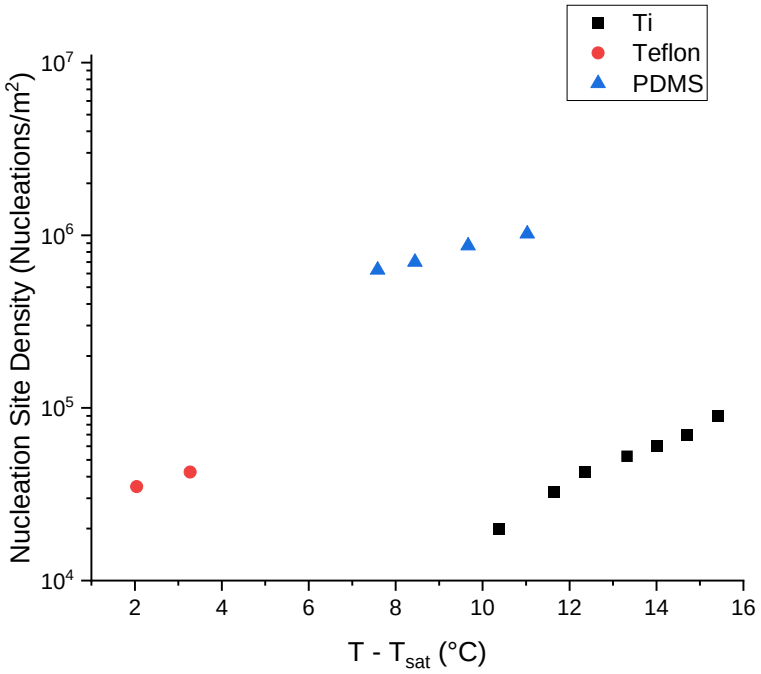


Figure 4.7. Nucleation site density for the Ti, Teflon, and PDMS surfaces.

Fig. 4.8 shows the measurement of a single representative bubble contact diameter from an IR image for each of the surfaces, which was taken at the end of the receding stage where the contact diameter was at its maximum. The bounds of the contact diameter were indicated by a sharp difference in temperature across the interface. The PDMS surface had the smallest maximum contact diameter of the three surfaces at 1.1 mm, followed by the Ti surface at 2.9 mm, and the Teflon at 4.9 mm. The large contact diameter of the Teflon surface likely contributed to

the early onset of critical heat flux. Meanwhile, the small contact diameter of the PDMS surface likely improved the CHF performance compared to the Teflon surface.

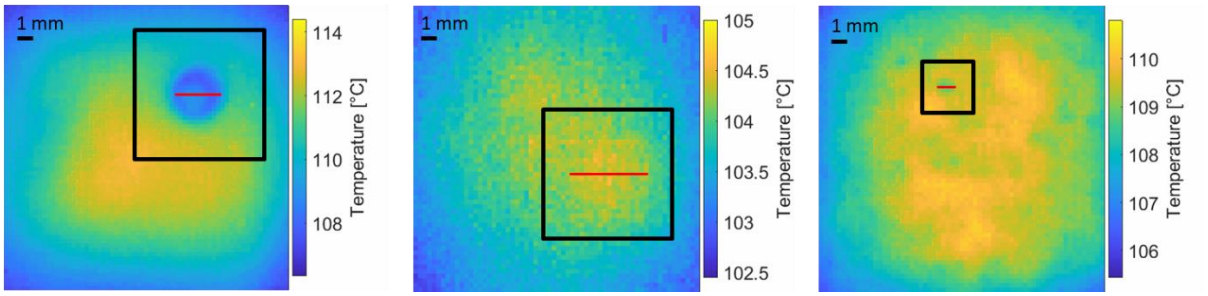


Figure . Maximum contact diameter for Ti (left), Teflon (middle), and PDMS (right) surfaces. The heat flux was at 8.5 W/cm$^2$ for the Ti, 2.1 W/cm$^2$ for the Teflon, and 28.3 W/cm$^2$ for the PDMS.

Finally, the total ebullition time was calculated for the three surfaces. For the Ti surface, the ebullition cycle was the most regular and nucleated from the same spot. Because of this, the ebullition cycle could clearly be plotted, and the temperature history of four points at different locations of the bubble from center outwards is shown in Fig. 4.9. The ebullition time was calculated as the average difference between nucleation events, which is indicated by the minimum temperatures of the center. From the plot, the average ebullition time was 53 ms. A noticeable waiting time between each bubble was observed, which suggested that full rewetting occurred after bubble departure. Furthermore, the center of the bubble growth sites did not cool as much as points away from the center, potentially suggesting dryout of the microlayer region in the center of the bubble.

To calculate the ebullition time for the Teflon and PDMS surfaces, a different approach was taken. Because the exact nucleation location varied slightly between nucleation events, unlike the Ti surface, the total ebullition time was calculated by playing the infrared video frame-by-frame and noting the moment at which the bubble departs. The ebullition time is calculated by corresponding the number of frames between departure events with frame rate, and an average of multiple ebullition times was taken. For the Teflon surface, the bubble departure was indicated by a sudden decrease in temperature, while for the PDMS surface, was indicated by a sudden increase in temperature. From these, the ebullition time for the Teflon surface is estimated to be 201 ms, and the ebullition time for the PDMS surface is 16 ms. The PDMS surface had the quickest

ebullition time, which contributed to its effective boiling performance. The long ebullition time of the Teflon surface allowed the bubble to dry out and form hot spots, contributing to the poor critical heat flux performance.

From observations in this study, the PDMS surface had the best performance because of its superior nucleation site density, bubble ebullition time, and maximum contact diameter. Dense bubble nucleation and short ebullition time are associated with better heat transfer due to the promotion of bubble formation in a given area and time, while the small maximum contact diameter prevented vapor spreading that would lead to critical heat flux. A summary of the findings is shown in Table 4.1.

The results of this study provide fundamental insights on the three boiling wettability regimes. For one, surfaces with wetting characteristics in the hygrophobic regime are not suitable for boiling applications because of their early onset of critical heat flux caused by vapor spreading, hot spot formation, and long ebullition times. However, the more important takeaways are with respect to boiling from surfaces having wetting characteristics in the hygrophilic and ambiphilic regimes. Although surfaces with hygrophilic characteristics experience higher per-bubble heat transfer due to microlayer evaporation, surfaces with ambiphilic characteristics experience an order of magnitude increase in nucleation site density and shorter ebullition times, leading to an overall lower surface temperature and better boiling performance. This suggests that the nucleation benefits of the ambiphilic regime significantly outweigh the benefits of increased microlayer evaporation in the hygrophilic regime.

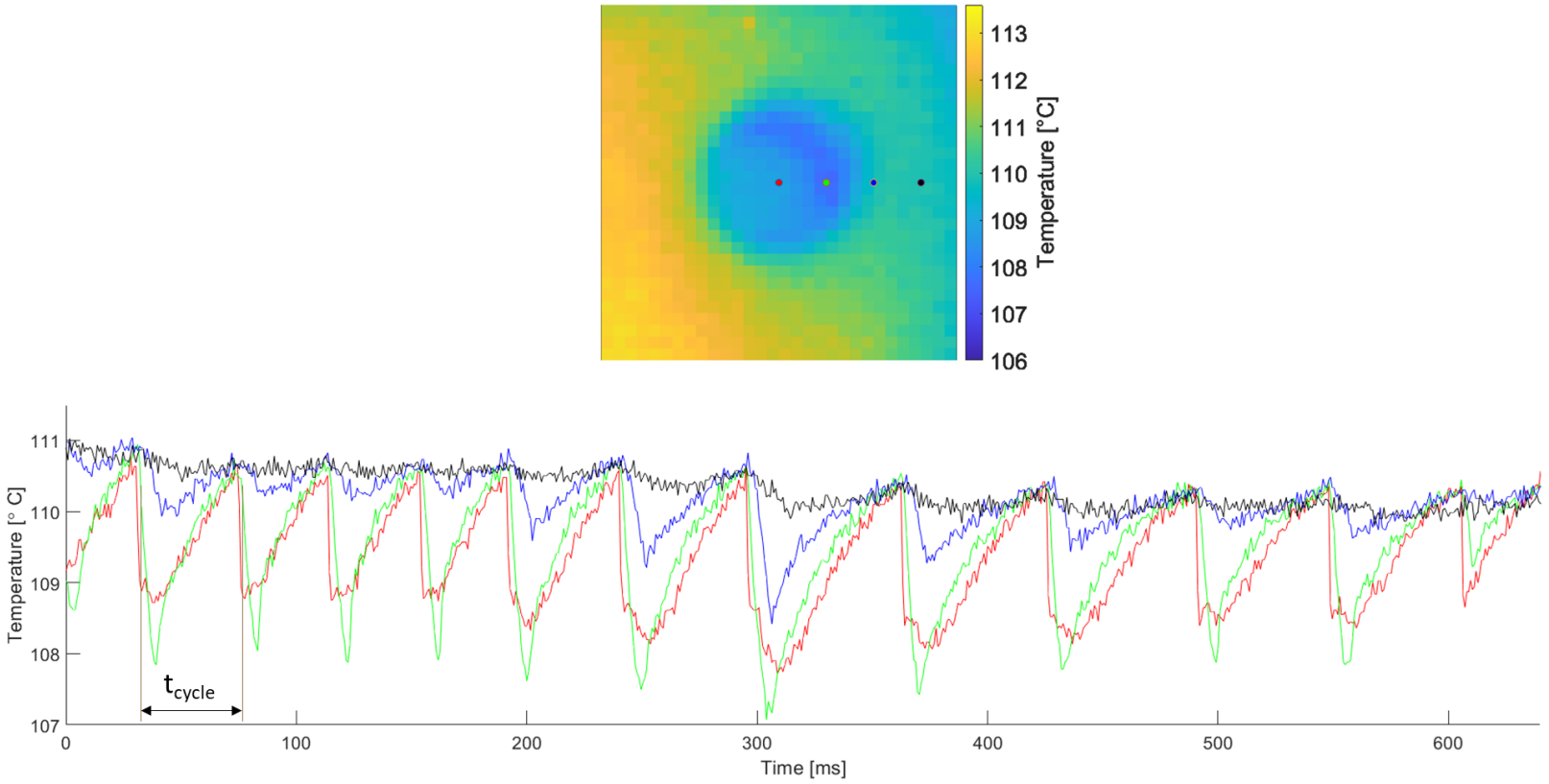


Figure 4.8. Temperature history at four points for the Ti surface across a single bubble at 8.5 W/cm$^2$. The center is indicated in red, followed by green, blue, and black outwards.

Table 4.1. Summary of key characteristics and findings.

| **Surface** | **Ti** | **Teflon** | **PDMS** |
|---|---|---|---|
| Advancing Angle (°) | 70.2 | 120.5 | 121.6 |
| Receding Angle (°) | ~10 | 107.6 | 39.0 |
| Boiling Curve | Worst at low heat fluxes, decent overall due to higher CHF than Teflon due to rewetting and waiting time. | Effective at low heat fluxes due to bubble formation and low waiting time caused by pinching. However, it reached CHF prematurely due to long ebullition times, large contact diameters, and hot spots. | Most effective overall due to nucleation site density, bubble ebullition time, maximum contact diameter, and short waiting times due to pinching. |
| Nucleation Site Density (nucleations/$m^2$) | $10^4$-$10^5$ from a 10-15 °C superheat | $10^4$-$10^5$ from a 2-3 °C superheat | $10^5$-$10^6$ from an 8-11 °C superheat |
| Bubble Ebullition Time (ms) | 53 | 201 | 16 |
| Maximum Contact Diameter (mm) | 2.9 | 4.9 | 1.1 |

# 5. CONCLUSIONS AND FUTURE WORK

Dynamic wettability has been shown to be the primary indicator for boiling performance. Using high-speed infrared thermography and high-speed flow visualizations, various aspects of the boiling process were observed and compared for surfaces having differing dynamic wettabilities. The flow visualizations were used to assess the contact line mechanics and observe other qualitative attributes of the boiling process. The infrared temperature maps were used to quantitatively assess boiling performance and nucleation characteristics such as nucleation site density, nucleation time, and maximum bubble diameter.

Three surfaces were fabricated with dynamic contact angles representative of the three boiling wettability regimes with water. The Ti surfaces, with both advancing and receding contact angles below 90°, was representative of the hygrophilic regime. The Teflon coated surface with both advancing and receding contact angles above 90°, was representative of the hygrophobic regime. The PDMS coated surfaces with advancing contact angle over 90° and receding contact angle below 90° was representative of the ambiphilic regime. From the boiling curves, the PDMS surface had the highest heat transfer coefficient and lowest superheats, and this was due to the order of magnitude greater nucleation site density, the shortest total ebullition time, and the smallest contact diameter. The high nucleation site density and short ebullition time allowed the highly effective heat transfer that comes with bubble formation to occur consistently and over a large portion of the surface; critical heat flux was avoided by minimizing the contact with surface. The Ti surface had poor heat transfer performance at early heat fluxes with the highest superheats and lowest heat transfer coefficient, but the surface avoided the early onset of critical heat flux as with the Teflon surface, allowing better relative performance at higher heat fluxes.. Both the poor relative performance and critical heat flux avoidance were caused by the waiting time between bubbles: the rewetting prevented effective heat transfer associated with contact line motion while also preventing dryout. Finally, the Teflon surface performed well at low heat fluxes due to its proclivity to form bubbles and small waiting time due to pinch off during bubble departure. However, these bubbles quickly covered the surface and caused early critical heat flux due to their large size resulting from a large receding contact angle, long ebullition times, and dryout under the bubble, and this led to an early critical heat flux.

This study was able to experimentally characterize the performance of surfaces spanning the three regimes of dynamic wettabilities in boiling, as well as explain the mechanisms that led to their relative performance differences. By measuring temperature with infrared from the bottom, new insights on the nucleation characteristics were made on the surfaces that were not possible with traditional visualization. Furthermore, nucleation characteristics such as the nucleation site density were found to play a significant role in boiling performance. This was the reason the ambiphilic case outperformed the hygrophilic case despite having less microlayer heat transfer; nucleation benefits of ambiphilic outweighed those of higher per-bubble heat transfer. Using this framework, researchers have a better understanding of what to strive for in engineering surfaces to achieve performance they require. Furthermore, this study opens the door for further investigations into dynamic wettability and boiling.

Further studies should explore specific attributes of boiling from surfaces in the ambiphilic regime, such as exploring the contributions of various heat transfer mechanisms and exploring the geometry of the microlayer. Furthermore, as this study investigated only a single surface within each wettability regime, testing additional surfaces within each regime would provide further understanding of how each dynamic contact angle impacts boiling performance within a given regime. With this deeper understanding, empirical models for heat transfer can be developed integrating the effects of dynamic wettability. Finally, developing novel surfaces based on the concept of ambiphilicity, such as biomimicking the wettability of a naturally ambiphilic rose petal, could lead to high-performance surfaces and provide deeper insight on the role of dynamic wettability.

# REFERENCES


[1] I. Mudawar, "Assessment of high-heat-flux thermal management schemes," *IEEE Trans. Compon. Packag. Technol.*, vol. 24, no. 2, pp. 122–141, 2001, doi: 10.1109/6144.926375.

[2] S. Fan and F. Duan, "A review of two-phase submerged boiling in thermal management of electronic cooling," *Int. J. Heat Mass Transf.*, vol. 150, p. 119324, Apr. 2020, doi: 10.1016/j.ijheatmasstransfer.2020.119324.

[3] S. M. Sohel Murshed and C. A. Nieto de Castro, "A critical review of traditional and emerging techniques and fluids for electronics cooling," *Renew. Sustain. Energy Rev.*, vol. 78, pp. 821–833, Oct. 2017, doi: 10.1016/j.rser.2017.04.112.

[4] S. H. Fuller and L. I. Millett, "Computing Performance: Game Over or Next Level?," *Computer*, vol. 44, no. 1, pp. 31–38, Jan. 2011, doi: 10.1109/MC.2011.15.

[5] M. Pedram and S. Nazarian, "Thermal Modeling, Analysis, and Management in VLSI Circuits: Principles and Methods," *Proc. IEEE*, vol. 94, no. 8, pp. 1487–1501, Aug. 2006, doi: 10.1109/JPROC.2006.879797.

[6] A. Shehabi *et al.*, "United States Data Center Energy Usage Report," LBNL--1005775, 1372902, Jun. 2016. doi: 10.2172/1372902.

[7] S. V. Garimella, T. Persoons, J. Weibel, and L.-T. Yeh, "Technological drivers in data centers and telecom systems: Multiscale thermal, electrical, and energy management," *Appl. Energy*, vol. 107, pp. 66–80, Jul. 2013, doi: 10.1016/j.apenergy.2013.02.047.

[8] G. Liang and I. Mudawar, "Review of pool boiling enhancement by surface modification," *Int. J. Heat Mass Transf.*, vol. 128, pp. 892–933, Jan. 2019, doi: 10.1016/j.ijheatmasstransfer.2018.09.026.

[9] Y. Takata *et al.*, "Effect of surface wettability on boiling and evaporation," *Energy*, vol. 30, no. 2, pp. 209–220, Feb. 2005, doi: 10.1016/j.energy.2004.05.004.

[10] A. R. Girard, J. Kim, and S. M. You, "Pool Boiling Heat Transfer of Water on Hydrophilic Surfaces With Different Wettability," in *Volume 8: Heat Transfer and Thermal Engineering*, Phoenix, Arizona, USA, Nov. 2016, p. V008T10A018, doi: 10.1115/IMECE2016-67294.

[11] H. Jo, H. S. Ahn, S. Kang, and M. H. Kim, "A study of nucleate boiling heat transfer on hydrophilic, hydrophobic and heterogeneous wetting surfaces," *Int. J. Heat Mass Transf.*, vol. 54, no. 25, pp. 5643–5652, Dec. 2011, doi: 10.1016/j.ijheatmasstransfer.2011.06.001.

[12] N. Mohammadi, D. Fadda, C. K. Choi, J. Lee, and S. M. You, "Effects of surface wettability on pool boiling of water using super-polished silicon surfaces," *Int. J. Heat Mass Transf.*, vol. 127, pp. 1128–1137, Dec. 2018, doi: 10.1016/j.ijheatmasstransfer.2018.07.122.

[13]Y. Takata, S. Hidaka, and T. Uraguchi, "Boiling Feature on a Super Water-Repellent Surface," *Heat Transf. Eng.*, vol. 27, no. 8, pp. 25–30, Sep. 2006, doi: 10.1080/01457630600793962.

[14] H. T. Phan, N. Caney, P. Marty, S. Colasson, and J. Gavillet, "Surface wettability control by nanocoating: The effects on pool boiling heat transfer and nucleation mechanism," *Int. J. Heat Mass Transf.*, vol. 52, no. 23, pp. 5459–5471, Nov. 2009, doi: 10.1016/j.ijheatmasstransfer.2009.06.032.

[15] T. P. Allred, J. A. Weibel, and S. V. Garimella, "Enabling Highly Effective Boiling from Superhydrophobic Surfaces," *Phys. Rev. Lett.*, vol. 120, no. 17, p. 174501, Apr. 2018, doi: 10.1103/PhysRevLett.120.174501.

[16] T. P. Allred, J. A. Weibel, and S. V. Garimella, “The petal effect of parahydrophobic surfaces offers low receding contact angles that promote effective boiling,” *Int. J. Heat Mass Transf.*, vol. 135, pp. 403–412, Jun. 2019, doi: 10.1016/j.ijheatmasstransfer.2019.02.002.
[17] T. P. Allred, “Effects of Dynamic Surface Wettability on Pool Boiling Behavior,” Ph.D dissertation, Purdue University Graduate School, 2019.
[18] J. Kim, “Review of nucleate pool boiling bubble heat transfer mechanisms,” *Int. J. Multiph. Flow*, vol. 35, no. 12, pp. 1067–1076, Dec. 2009, doi: 10.1016/j.ijmultiphaseflow.2009.07.008.
[19] W. M. Rohsenow, “A method of correlating heat transfer data for surface boiling of liquids,” Cambridge, Mass. : M.I.T. Division of Industrial Cooperation, [1951], Technical Report, 1951.
[20] V. P. Carey, *Liquid-vapor phase-change phenomena: an introduction to the thermophysics of vaporization and condensation processes in heat transfer equipment*. CRC Press, 2020.
[21] K. Forster and R. Greif, “Heat Transfer to a Boiling Liquid Mechanism and Correlations,” California. Univ., Los Angeles, CA (United States). Dept. of Engineering, AECU-3843, May 1958. doi: 10.2172/4298039.
[22] H. K. Forster and N. Zuber, “Dynamics of vapor bubbles and boiling heat transfer,” *AIChE J.*, vol. 1, no. 4, pp. 531–535, 1955, doi: 10.1002/aic.690010425.
[23] S. Jung and H. Kim, “An experimental method to simultaneously measure the dynamics and heat transfer associated with a single bubble during nucleate boiling on a horizontal surface,” *Int. J. Heat Mass Transf.*, vol. 73, pp. 365–375, Jun. 2014, doi: 10.1016/j.ijheatmasstransfer.2014.02.014.
[24] B. B. Mikic and W. M. Rohsenow, “A New Correlation of Pool-Boiling Data Including the Effect of Heating Surface Characteristics,” *J. Heat Transf.*, vol. 91, no. 2, pp. 245–250, May 1969, doi: 10.1115/1.3580136.
[25] F. D. Moore and R. B. Mesler, “The measurement of rapid surface temperature fluctuations during nucleate boiling of water,” *AIChE J.*, vol. 7, no. 4, pp. 620–624, 1961, doi: 10.1002/aic.690070418.
[26] Z. Chen, A. Haginiwa, and Y. Utaka, “Detailed structure of microlayer in nucleate pool boiling for water measured by laser interferometric method,” *Int. J. Heat Mass Transf.*, vol. 108, pp. 1285–1291, May 2017, doi: 10.1016/j.ijheatmasstransfer.2017.01.003.
[27] Z. Chen, X. Hu, K. Hu, Y. Utaka, and S. Mori, “Measurement of the microlayer characteristics in the whole range of nucleate boiling for water by laser interferometry,” *Int. J. Heat Mass Transf.*, vol. 146, p. 118856, Jan. 2020, doi: 10.1016/j.ijheatmasstransfer.2019.118856.
[28] Y. Utaka, K. Hu, Z. Chen, and T. Morokuma, “Measurement of contribution of microlayer evaporation applying the microlayer volume change during nucleate pool boiling for water and ethanol,” *Int. J. Heat Mass Transf.*, vol. 125, pp. 243–247, Oct. 2018, doi: 10.1016/j.ijheatmasstransfer.2018.04.044.
[29] R. L. Judd and K. S. Hwang, “A Comprehensive Model for Nucleate Pool Boiling Heat Transfer Including Microlayer Evaporation,” *J. Heat Transf.*, vol. 98, no. 4, pp. 623–629, Nov. 1976, doi: 10.1115/1.3450610.
[30] P. C. Wayner, Y. K. Kao, and L. V. LaCroix, “The interline heat-transfer coefficient of an evaporating wetting film,” *Int. J. Heat Mass Transf.*, vol. 19, no. 5, pp. 487–492, May 1976, doi: 10.1016/0017-9310(76)90161-7.

[31] P. Stephan and J. Hammer, “A new model for nucleate boiling heat transfer,” *Wärme-Stoffübertrag.*, vol. 30, no. 2, pp. 119–125, Nov. 1994, doi: 10.1007/BF00715018.
[32] E. Wagner and P. Stephan, “High-Resolution Measurements at Nucleate Boiling of Pure FC-84 and FC-3284 and Its Binary Mixtures,” *J. Heat Transf.*, vol. 131, no. 12, Dec. 2009, doi: 10.1115/1.3220143.
[33] S. Moghaddam and K. Kiger, “Physical mechanisms of heat transfer during single bubble nucleate boiling of FC-72 under saturation conditions-I. Experimental investigation,” *Int. J. Heat Mass Transf.*, vol. 52, no. 5, pp. 1284–1294, Feb. 2009, doi: 10.1016/j.ijheatmasstransfer.2008.08.018.
[34] S. Moghaddam and K. Kiger, “Physical mechanisms of heat transfer during single bubble nucleate boiling of FC-72 under saturation conditions. II: Theoretical analysis,” *Int. J. Heat Mass Transf.*, vol. 52, no. 5, pp. 1295–1303, Feb. 2009, doi: 10.1016/j.ijheatmasstransfer.2008.08.024.
[35] T. Yabuki and O. Nakabeppu, “Heat transfer mechanisms in isolated bubble boiling of water observed with MEMS sensor,” *Int. J. Heat Mass Transf.*, vol. 76, pp. 286–297, Sep. 2014, doi: 10.1016/j.ijheatmasstransfer.2014.04.012.
[36] G. Liang and I. Mudawar, “Pool boiling critical heat flux (CHF) – Part 1: Review of mechanisms, models, and correlations,” *Int. J. Heat Mass Transf.*, vol. 117, pp. 1352–1367, Feb. 2018, doi: 10.1016/j.ijheatmasstransfer.2017.09.134.
[37] G. Liang and I. Mudawar, “Pool boiling critical heat flux (CHF) – Part 2: Assessment of models and correlations,” *Int. J. Heat Mass Transf.*, vol. 117, pp. 1368–1383, Feb. 2018, doi: 10.1016/j.ijheatmasstransfer.2017.09.073.
[38] D. C. Groeneveld *et al.*, “The 2006 CHF look-up table,” *Nucl. Eng. Des.*, vol. 237, no. 15–17, pp. 1909–1922, Sep. 2007, doi: 10.1016/j.nucengdes.2007.02.014.
[39] S. Xie, M. Shahmohammadi Beni, J. Cai, and J. Zhao, “Review of critical-heat-flux enhancement methods,” *Int. J. Heat Mass Transf.*, vol. 122, pp. 275–289, Jul. 2018, doi: 10.1016/j.ijheatmasstransfer.2018.01.116.
[40] N. Zuber, “Hydrodynamic Aspects Of Boiling Heat Transfer (Thesis),” AECU--4439, 4175511, Jun. 1959. doi: 10.2172/4175511.
[41] N. Zuber, “The dynamics of vapor bubbles in nonuniform temperature fields,” *Int. J. Heat Mass Transf.*, vol. 2, no. 1–2, pp. 83–98, Mar. 1961, doi: 10.1016/0017-9310(61)90016-3.
[42] J. Kim, S. Jun, R. Laksnarain, and S. M. You, “Effect of surface roughness on pool boiling heat transfer at a heated surface having moderate wettability,” *Int. J. Heat Mass Transf.*, vol. 101, pp. 992–1002, Oct. 2016, doi: 10.1016/j.ijheatmasstransfer.2016.05.067.
[43] W. M. Rohsenow and P. Griffith, “Correlation of Maximum Heat Flux Data for Boiling of Saturated Liquids,” p. 13.
[44] Y. Haramura and Y. Katto, “A new hydrodynamic model of critical heat flux, applicable widely to both pool and forced convection boiling on submerged bodies in saturated liquids,” *Int. J. Heat Mass Transf.*, vol. 26, no. 3, pp. 389–399, Mar. 1983, doi: 10.1016/0017-9310(83)90043-1.
[45] V. V. Yagov, “Is a crisis in pool boiling actually a hydrodynamic phenomenon?,” *Int. J. Heat Mass Transf.*, vol. 73, pp. 265–273, Jun. 2014, doi: 10.1016/j.ijheatmasstransfer.2014.01.076.
[46] T. G. Theofanous, T. N. Dinh, J. P. Tu, and A. T. Dinh, “The boiling crisis phenomenon: Part II: dryout dynamics and burnout,” *Exp. Therm. Fluid Sci.*, vol. 26, no. 6, pp. 793–810, Aug. 2002, doi: 10.1016/S0894-1777(02)00193-0.

[47] J. E. Galloway and I. Mudawar, “CHF mechanism in flow boiling from a short heated wall—II. Theoretical CHF model,” *Int. J. Heat Mass Transf.*, vol. 36, no. 10, pp. 2527–2540, Jul. 1993, doi: 10.1016/S0017-9310(05)80191-7.
[48] C.-K. Guan, J. F. Klausner, and R. Mei, “A new mechanistic model for pool boiling CHF on horizontal surfaces,” *Int. J. Heat Mass Transf.*, vol. 54, no. 17, pp. 3960–3969, Aug. 2011, doi: 10.1016/j.ijheatmasstransfer.2011.04.029.
[49] M. Jakob, “Heat transfer in evaporation and condensation,” *Mech Eng*, vol. 58, pp. 729–739, 1936.
[50] H. M. Kurihara and J. E. Myers, “The effects of superheat and surface roughness on boiling coefficients,” *AIChE J.*, vol. 6, no. 1, pp. 83–91, 1960, doi: 10.1002/aic.690060117.
[51] S. T. Hsu and F. W. Schmidt, “Measured Variations in Local Surface Temperatures in Pool Boiling of Water,” *J. Heat Transf.*, vol. 83, no. 3, pp. 254–260, Aug. 1961, doi: 10.1115/1.3682252.
[52] P. J. Marto and W. M. Rohsenow, “Effects of Surface Conditions on Nucleate Pool Boiling of Sodium,” *J. Heat Transf.*, vol. 88, no. 2, pp. 196–203, May 1966, doi: 10.1115/1.3691514.
[53] B. J. Jones, J. P. McHale, and S. V. Garimella, “The Influence of Surface Roughness on Nucleate Pool Boiling Heat Transfer,” *J. Heat Transf.*, vol. 131, no. 12, Dec. 2009, doi: 10.1115/1.3220144.
[54] A. E. Bergles and M. C. Chyu, “Characteristics of Nucleate Pool Boiling From Porous Metallic Coatings,” *J. Heat Transf.*, vol. 104, no. 2, pp. 279–285, May 1982, doi: 10.1115/1.3245084.
[55] S. Sarangi, J. A. Weibel, and S. V. Garimella, “Effect of particle size on surface-coating enhancement of pool boiling heat transfer,” *Int. J. Heat Mass Transf.*, vol. 81, pp. 103–113, Feb. 2015, doi: 10.1016/j.ijheatmasstransfer.2014.09.052.
[56] S. Sarangi, J. A. Weibel, and S. V. Garimella, “Quantitative Evaluation of the Dependence of Pool Boiling Heat Transfer Enhancement on Sintered Particle Coating Characteristics,” *J. Heat Transf.*, vol. 139, no. 2, p. 021502, Feb. 2017, doi: 10.1115/1.4034901.
[57] X. Ji, J. Xu, Z. Zhao, and W. Yang, “Pool boiling heat transfer on uniform and non-uniform porous coating surfaces,” *Exp. Therm. Fluid Sci.*, vol. 48, pp. 198–212, Jul. 2013, doi: 10.1016/j.expthermflusci.2013.03.002.
[58] T. M. Anderson and I. Mudawar, “Microelectronic Cooling by Enhanced Pool Boiling of a Dielectric Fluorocarbon Liquid,” *J. Heat Transf.*, vol. 111, no. 3, pp. 752–759, Aug. 1989, doi: 10.1115/1.3250747.
[59] H. Honda, H. Takamatsu, and J. J. Wei, “Enhanced boiling of FC-72 on silicon chips with micro-pin-fins and submicron-scale roughness,” *J. Heat Transf.*, vol. 124, no. 2, pp. 383–390, 2002, doi: 10.1115/1.1447937.
[60] A. Zou, D. P. Singh, and S. C. Maroo, “Early Evaporation of Microlayer for Boiling Heat Transfer Enhancement,” *Langmuir*, vol. 32, no. 42, pp. 10808–10814, Oct. 2016, doi: 10.1021/acs.langmuir.6b02642.
[61] T. Young, “III. An essay on the cohesion of fluids,” *Philos. Trans. R. Soc. Lond.*, vol. 95, pp. 65–87, Jan. 1805, doi: 10.1098/rstl.1805.0005.
[62] T. Huhtamäki, X. Tian, J. T. Korhonen, and R. H. A. Ras, “Surface-wetting characterization using contact-angle measurements,” *Nat. Protoc. Lond.*, vol. 13, no. 7, pp. 1521–1538, Jul. 2018, doi: http://dx.doi.org.ezproxy.lib.purdue.edu/10.1038/s41596-018-0003-z.

[63] T. Darmanin, E. T. de Givenchy, S. Amigoni, and F. Guittard, “Superhydrophobic Surfaces by Electrochemical Processes,” *Adv. Mater.*, vol. 25, no. 10, pp. 1378–1394, 2013, doi: 10.1002/adma.201204300.
[64] A. Marmur, “Solid-Surface Characterization by Wetting,” *Annu. Rev. Mater. Res.*, vol. 39, no. 1, pp. 473–489, Jul. 2009, doi: 10.1146/annurev.matsci.38.060407.132425.
[65] K. L. Mittal, *Contact Angle, Wettability and Adhesion, Volume 6*. CRC Press, 2009.
[66] L. Gao and T. J. McCarthy, “Contact Angle Hysteresis Explained,” *Langmuir*, vol. 22, no. 14, pp. 6234–6237, Jul. 2006, doi: 10.1021/la060254j.
[67] A. Marmur, “From Hygrophilic to Superhygrophobic: Theoretical Conditions for Making High-Contact-Angle Surfaces from Low-Contact-Angle Materials,” *Langmuir*, vol. 24, no. 14, pp. 7573–7579, Jul. 2008, doi: 10.1021/la800304r.
[68] P.-G. de Gennes, F. Brochard-Wyart, and D. Quéré, *Capillarity and wetting phenomena: drops, bubbles, pearls, waves*. New York, NY: Springer, 2010.
[69] R. N. Wenzel, “Resistance of Solid Surfaces to Wetting by Water,” *Ind. Eng. Chem.*, vol. 28, no. 8, pp. 988–994, Aug. 1936, doi: 10.1021/ie50320a024.
[70] R. N. Wenzel, “Surface Roughness and Contact Angle.,” *J. Phys. Colloid Chem.*, vol. 53, no. 9, pp. 1466–1467, Sep. 1949, doi: 10.1021/j150474a015.
[71] J. Bico, U. Thiele, and D. Quéré, “Wetting of textured surfaces,” *Colloids Surf. Physicochem. Eng. Asp.*, vol. 206, no. 1–3, pp. 41–46, Jul. 2002, doi: 10.1016/S0927-7757(02)00061-4.
[72] A. B. D. Cassie and S. Baxter, “Wettability of porous surfaces,” *Trans. Faraday Soc.*, vol. 40, no. 0, pp. 546–551, Jan. 1944, doi: 10.1039/TF9444000546.
[73] C. Dorrer and J. Rühe, “Some thoughts on superhydrophobic wetting,” *Soft Matter*, vol. 5, no. 1, pp. 51–61, Dec. 2008, doi: 10.1039/B811945G.
[74] A. Marmur, “Wetting on Hydrophobic Rough Surfaces: To Be Heterogeneous or Not To Be?,” *Langmuir*, vol. 19, no. 20, pp. 8343–8348, Sep. 2003, doi: 10.1021/la0344682.
[75] C. R. Szczepanski, F. Guittard, and T. Darmanin, “Recent advances in the study and design of parahydrophobic surfaces: From natural examples to synthetic approaches,” *Adv. Colloid Interface Sci.*, vol. 241, pp. 37–61, Mar. 2017, doi: 10.1016/j.cis.2017.01.002.
[76] L. Feng *et al.*, “Petal Effect: A Superhydrophobic State with High Adhesive Force,” *Langmuir*, vol. 24, no. 8, pp. 4114–4119, Apr. 2008, doi: 10.1021/la703821h.
[77] H. Jin, Y. Li, P. Zhang, S. Nie, and N. Gao, “The investigation of the wetting behavior on the red rose petal,” *Appl. Phys. Lett.*, vol. 108, no. 15, p. 151605, Apr. 2016, doi: 10.1063/1.4947057.
[78] J. Wang, Q. Yang, M. Wang, C. Wang, and L. Jiang, “Rose petals with a novel and steady air bubble pinning effect in aqueous media,” *Soft Matter*, vol. 8, no. 7, pp. 2261–2266, Jan. 2012, doi: 10.1039/C2SM06705F.
[79] A. R. Betz, J. Jenkins, C.-J. “CJ” Kim, and D. Attinger, “Boiling heat transfer on superhydrophilic, superhydrophobic, and superbiphilic surfaces,” *Int. J. Heat Mass Transf.*, vol. 57, no. 2, pp. 733–741, Feb. 2013, doi: 10.1016/j.ijheatmasstransfer.2012.10.080.
[80] M. M. Rahman, E. Ölçeroğlu, and M. McCarthy, “Role of Wickability on the Critical Heat Flux of Structured Superhydrophilic Surfaces,” *Langmuir*, vol. 30, no. 37, pp. 11225–11234, Sep. 2014, doi: 10.1021/la5030923.
[81] N. S. Dhillon, J. Buongiorno, and K. K. Varanasi, “Critical heat flux maxima during boiling crisis on textured surfaces,” *Nat. Commun.*, vol. 6, no. 1, p. 8247, Nov. 2015, doi: 10.1038/ncomms9247.

[82] H. S. Ahn, H. J. Jo, S. H. Kang, and M. H. Kim, “Effect of liquid spreading due to nano/microstructures on the critical heat flux during pool boiling,” *Appl. Phys. Lett.*, vol. 98, no. 7, p. 071908, Feb. 2011, doi: 10.1063/1.3555430.
[83] K.-H. Chu, Y. Soo Joung, R. Enright, C. R. Buie, and E. N. Wang, “Hierarchically structured surfaces for boiling critical heat flux enhancement,” *Appl. Phys. Lett.*, vol. 102, no. 15, p. 151602, Apr. 2013, doi: 10.1063/1.4801811.
[84] C.-C. Hsu and P.-H. Chen, “Surface wettability effects on critical heat flux of boiling heat transfer using nanoparticle coatings,” *Int. J. Heat Mass Transf.*, vol. 55, no. 13, pp. 3713–3719, Jun. 2012, doi: 10.1016/j.ijheatmasstransfer.2012.03.003.
[85] I. Malavasi, B. Bourdon, P. Di Marco, J. de Coninck, and M. Marengo, “Appearance of a low superheat ‘quasi-Leidenfrost’ regime for boiling on superhydrophobic surfaces,” *Int. Commun. Heat Mass Transf.*, vol. 63, pp. 1–7, Apr. 2015, doi: 10.1016/j.icheatmasstransfer.2015.01.012.
[86] C. R. Kharangate and I. Mudawar, “Review of computational studies on boiling and condensation,” *Int. J. Heat Mass Transf.*, vol. 108, pp. 1164–1196, May 2017, doi: 10.1016/j.ijheatmasstransfer.2016.12.065.
[87] G. Son, V. K. Dhir, and N. Ramanujapu, “Dynamics and Heat Transfer Associated With a Single Bubble During Nucleate Boiling on a Horizontal Surface,” *J. Heat Transf.*, vol. 121, no. 3, pp. 623–631, Aug. 1999, doi: 10.1115/1.2826025.
[88] A. Mukherjee and S. Kandlikar, “Effect of Dynamic Contact Angle on Single Bubbles During Nucleate Pool Boiling,” Jan. 2004, vol. 375, doi: 10.1115/IMECE2004-59976.
[89] A. Mukherjee and S. G. Kandlikar, “Numerical study of single bubbles with dynamic contact angle during nucleate pool boiling,” *Int. J. Heat Mass Transf.*, vol. 50, no. 1, pp. 127–138, Jan. 2007, doi: 10.1016/j.ijheatmasstransfer.2006.06.037.
[90] Y. Chen, R. Mertz, and R. Kulenovic, “Numerical simulation of bubble formation on orifice plates with a moving contact line,” *Int. J. Multiph. Flow*, vol. 35, no. 1, pp. 66–77, Jan. 2009, doi: 10.1016/j.ijmultiphaseflow.2008.07.007.
[91] T. G. Theofanous, J. P. Tu, A. T. Dinh, and T. N. Dinh, “The boiling crisis phenomenon: Part I: nucleation and nucleate boiling heat transfer,” *Exp. Therm. Fluid Sci.*, vol. 26, no. 6, pp. 775–792, Aug. 2002, doi: 10.1016/S0894-1777(02)00192-9.
[92] I. Golobic, J. Petkovsek, M. Baselj, A. Papez, and D. B. R. Kenning, “Experimental determination of transient wall temperature distributions close to growing vapor bubbles,” *Heat Mass Transf.*, vol. 45, no. 7, pp. 857–866, May 2009, doi: 10.1007/s00231-007-0295-y.
[93] I. Golobic, J. Petkovsek, and D. B. R. Kenning, “Bubble growth and horizontal coalescence in saturated pool boiling on a titanium foil, investigated by high-speed IR thermography,” *Int. J. Heat Mass Transf.*, vol. 55, no. 4, pp. 1385–1402, Jan. 2012, doi: 10.1016/j.ijheatmasstransfer.2011.08.021.
[94] I. Golobič and H. Gjerkeš, “Interactions between laser-activated nucleation sites in pool boiling,” *Int. J. Heat Mass Transf.*, vol. 44, no. 1, pp. 143–153, Jan. 2001, doi: 10.1016/S0017-9310(00)00087-9.
[95] J. Voglar, M. Zupančič, A. Peperko, P. Birbarah, N. Miljkovic, and I. Golobič, “Analysis of heater-wall temperature distributions during the saturated pool boiling of water,” *Exp. Therm. Fluid Sci.*, vol. 102, pp. 205–214, Apr. 2019, doi: 10.1016/j.expthermflusci.2018.11.012.

[96] S. Fischer, S. Herbert, A. Sielaff, E. M. Slomski, P. Stephan, and M. Oechsner, "Experimental Investigation of Nucleate Boiling on a Thermal Capacitive Heater Under Variable Gravity Conditions," *Microgravity Sci. Technol.*, vol. 24, no. 3, pp. 139–146, Jun. 2012, doi: 10.1007/s12217-011-9273-6.

[97] P. Stephan, A. Sielaff, S. Fischer, J. Dietl, and S. Herbert, "A contribution to the basic understanding of nucleate boiling phenomena: generic experiments and numerical simulations," 2013, doi: 10.11368/tse.21.39.

[98] C. Gerardi, J. Buongiorno, L. Hu, and T. McKrell, "Study of bubble growth in water pool boiling through synchronized, infrared thermometry and high-speed video," *Int. J. Heat Mass Transf.*, vol. 53, no. 19, pp. 4185–4192, Sep. 2010, doi: 10.1016/j.ijheatmasstransfer.2010.05.041.

[99] X. Duan, B. Phillips, T. McKrell, and J. Buongiorno, "Synchronized High-Speed Video, Infrared Thermometry, and Particle Image Velocimetry Data for Validation of Interface-Tracking Simulations of Nucleate Boiling Phenomena," *Exp. Heat Transf.*, vol. 26, no. 2–3, pp. 169–197, Mar. 2013, doi: 10.1080/08916152.2012.736837.

[100] J. Jung, S. J. Kim, and J. Kim, "Observations of the Critical Heat Flux Process During Pool Boiling of FC-72," *J. Heat Transf.*, vol. 136, no. 4, Apr. 2014, doi: 10.1115/1.4025697.

[101] S. Jung and H. Kim, "An Experimental Study on Heat Transfer Mechanisms in the Microlayer using Integrated Total Reflection, Laser Interferometry and Infrared Thermometry Technique," *Heat Transf. Eng.*, vol. 36, no. 12, pp. 1002–1012, Aug. 2015, doi: 10.1080/01457632.2015.979109.

[102] S. Jung and H. Kim, "Hydrodynamic formation of a microlayer underneath a boiling bubble," *Int. J. Heat Mass Transf.*, vol. 120, pp. 1229–1240, May 2018, doi: 10.1016/j.ijheatmasstransfer.2017.12.098.

[103] M. Tetreault-Friend, "Systematic investigation of the effects of hydrophilic porosity on boiling heat transfer and critical heat flux," Thesis, Massachusetts Institute of Technology, 2014.

[104] J. Yoo, C. E. Estrada-Perez, and Y. A. Hassan, "An accurate wall temperature measurement using infrared thermometry with enhanced two-phase flow visualization in a convective boiling system," *Int. J. Therm. Sci.*, vol. 90, pp. 248–266, Apr. 2015, doi: 10.1016/j.ijthermalsci.2014.12.007.

[105] M. Kim and S. J. Kim, "Study on the Heat Transfer Mechanism in Nucleate Boiling of Water by Measuring Local Heat Flux and Temperature," in *2018 17th IEEE Intersociety Conference on Thermal and Thermomechanical Phenomena in Electronic Systems (ITherm)*, May 2018, pp. 620–629, doi: 10.1109/ITHERM.2018.8419612.

[106] L. D. Koffman and M. S. Plesset, "Experimental Observations of the Microlayer in Vapor Bubble Growth on a Heated Solid," *J. Heat Transf.*, vol. 105, no. 3, pp. 625–632, Aug. 1983, doi: 10.1115/1.3245631.

[107] M. Gao, L. Zhang, P. Cheng, and X. Quan, "An investigation of microlayer beneath nucleation bubble by laser interferometric method," *Int. J. Heat Mass Transf.*, vol. 57, no. 1, pp. 183–189, Jan. 2013, doi: 10.1016/j.ijheatmasstransfer.2012.10.017.

[108] S. Nishio and H. Tanaka, "Visualization of boiling structures in high heat–flux pool-boiling," *Int. J. Heat Mass Transf.*, vol. 47, no. 21, pp. 4559–4568, Oct. 2004, doi: 10.1016/j.ijheatmasstransfer.2003.07.033.

[109] R. C. Chu, R. E. Simons, M. J. Ellsworth, R. R. Schmidt, and V. Cozzolino, “Review of cooling technologies for computer products,” *IEEE Trans. Device Mater. Reliab.*, vol. 4, no. 4, pp. 568–585, Dec. 2004, doi: 10.1109/TDMR.2004.840855.
[110] H. Kim and J. Buongiorno, “Detection of liquid–vapor–solid triple contact line in two-phase heat transfer phenomena using high-speed infrared thermometry,” *Int. J. Multiph. Flow*, vol. 37, no. 2, pp. 166–172, Mar. 2011, doi: 10.1016/j.ijmultiphaseflow.2010.09.010.
[111] S. H. Kim, G. C. Lee, J. Y. Kang, H. S. Park, and M. H. Kim, “A study of nucleate bubble growth on microstructured surface through high speed and infrared visualization,” *Int. J. Multiph. Flow*, vol. 95, pp. 12–21, Oct. 2017, doi: 10.1016/j.ijmultiphaseflow.2017.02.007.
[112] M. Tariq, M. Abdelhamid, Y. Li, M. Omar, and Y. Zhou, “Fusion of Thermal and Visible Acquisitions for Evaluating Production-borne Scratches and Shunts in Photo-Voltaic PV Cells,” *J. Mater. Sci. Res.*, vol. 1, no. 4, Art. no. 4, Sep. 2012, doi: 10.5539/jmsr.v1n4p57.
[113] M. Bucci, A. Richenderfer, G.-Y. Su, T. McKrell, and J. Buongiorno, “A mechanistic IR calibration technique for boiling heat transfer investigations,” *Int. J. Multiph. Flow*, vol. 83, pp. 115–127, Jul. 2016, doi: 10.1016/j.ijmultiphaseflow.2016.03.007.

# VITA

Nicholas Vu received his Bachelor of Science (BS) in Mechanical Engineering and commissioned as an Ensign in the Navy from the United States Naval Academy in 2019. He completed his Master of Science in Mechanical Engineering (MSME) in 2020 at Purdue University under the advisement of Dr. Justin Weibel. He was awarded with funding from the Purdue Military Research Initiative. His research focuses on understanding the effects of dynamic wettability on boiling heat transfer. After graduating from Purdue, he will begin flight school in Pensacola, FL to begin a career as a Naval Aviator.